Multifunctional Cre-dependent transgenic mice for high-precision all-optical interrogation of neural circuits

Hayley A. Bounds[1,2*], Masato Sadahiro[1*], William D. Hendricks[1*], Marta Gajowa[1*], Ian Antón Oldenburg[1*], Karthika Gopakumar[1], Daniel Quintana[1], Bosiljka Tasic[3], Tanya L. Daigle[3], Hongkui Zeng[3], Hillel Adesnik[1,2,**]

[1]Department of Molecular and Cell Biology, University of California, Berkeley

[2]The Helen Wills Neuroscience Institute

[3]Allen Institute for Brain Science, Seattle, Washington

[*]These authors contributed equally to this work

[**]Corresponding author

Email: hadesnik@berkeley.edu

Abstract

Causally relating the detailed structure and function of neural circuits to behavior requires the ability to precisely and simultaneously write-in and read-out neural activity. All optical systems that combine two photon (2p) calcium imaging and targeted photostimulation provide such an approach, but require co-expression of an activity indicator, such as GCaMP, and an optogenetic actuator, ideally a potent soma-targeted opsin. In the mammalian brain, such co-expression has so far been achieved by viral transduction, which is invasive and can produce variable, focal, and sometimes toxic overexpression. To overcome this challenge, we developed and validated a Cre-reporter mouse ('Ai203') that conditionally expresses a soma-targeted opsin, ChroME, fused to GCaMP7s. 1p or 2p illumination of expressing neurons *in vitro* and *in vivo* produces powerful, precise activation comparable to viral expression of ChroME. The soma-targeted GCaMP7s provides sensitive activity measurements for tracking physiological activity, and the soma-targeted ChroME provides powerful control over neural ensemble activity with holographic optogenetics. We further demonstrate the use of the Ai203 reporter line in 1p optogenetic manipulation of performance on a cortex-dependent visual task and in 2p synaptic connectivity mapping. This new transgenic line could thus greatly facilitate the study of neural circuits by providing a flexible, convenient, and stable tool for all-optical access to large, cell-type specific neural populations throughout the nervous system.

Introduction

Multiphoton optogenetic techniques direct light to photostimulate neurons with near single-cell resolution and have been used to reveal basic rules of circuit connectivity and behavior (Adesnik & Abdeladim, 2021; Andrasfalvy et al., 2010; Bègue et al., 2013; Carrillo-Reid et al., 2016, 2019; I. W. Chen et al., 2019; Chettih & Harvey, 2019; Daie et al., 2021; Dalgleish et al., 2020; Gill et al., 2020; Lerman et al., 2019; Mardinly et al., 2018; Marshel et al., 2019; Naka et al., 2019; Packer et al., 2015; Papagiakoumou et al., 2010, 2020; Pégard et al., 2017; Rickgauer et al., 2014; Robinson et al., 2020; Ronzitti et al., 2018; Tasic et al., 2016; Yang et al., 2018). All-optical control of neural activity requires the co-expression of an opsin to "write in" activity and an activity indicator, usually GCaMP, to "read out" activity. The selection of opsin, indicator, and expression method are critical for determining the reliability, resolution, and scale of neural control.

Most studies have achieved the co-expression of an opsin and a calcium sensor using recombinant adeno-associated viruses (AAVs) (Carrillo-Reid et al., 2016, 2019; Chettih & Harvey, 2019; Daie et al., 2021; Dalgleish et al., 2020; Gill et al., 2020; Marshel et al., 2019; Naka et al., 2019; Rickgauer et al., 2014). Viral expression typically requires invasive surgery, produces heterogeneous expression across animals with variable spread, and can lead to toxic expression of the transgenes (Haery et al., 2019; Miyashita et al., 2013). In contrast, transgenic lines can provide robust, stable, and widespread expression (Daigle et al., 2018; Madisen et al., 2012, 2015; Wekselblatt et al., 2016). While many opsin-expressing transgenic lines exist, 2-photon (2p) photostimulation experiments have unique constraints and would benefit from a specialized line.

The optimal opsin construct for large-scale, precise 2p control of neural activity should allow power-efficient photostimulation and cellular scale resolution. 2p stimulation requires higher energy than 1-photon (1p) stimulation, so potent opsins are necessary to activate large ensembles of neurons without causing tissue damage (Mardinly et al., 2018; Picot et al., 2018). Several ultrapotent opsins, such as ChroME and ChRmine, have been developed for 2p optogenetics and enable simultaneous control of dozens of neurons (Mardinly et al., 2018; Marshel et al., 2019; Prakash et al., 2012). ChroME, which has extremely fast kinetics, can provide additional benefits, like minimizing unwanted activation from 2p imaging and allowing precise temporal control at high frequencies (Mardinly et al., 2018), similar to its parent opsin, Chronos (Klapoetke et al., 2014; Ronzitti et al., 2017). Soma-targeting the opsin improves the spatial resolution of stimulation (Baker et al., 2016; Forli et al., 2018; Mardinly et al., 2018; Shemesh et al., 2017; Wu et al., 2013). However, currently there are no transgenic lines that express ultrapotent opsins, nor any line that drives expression of a soma-targeted excitatory opsin. Such a line, particularly if it co-expressed an activity indicator such as GCaMP, would significantly facilitate 2p optogenetic experiments.

We present a new transgenic reporter line using the TIGRE2.0 system that conditionally co-expresses ChroME, an excitatory opsin, and GCaMP7s, a calcium indicator, as a single, soma-targeted fusion protein (Daigle et al., 2018; Dana et al., 2019; Mardinly et al., 2018). We thoroughly validate this line with a combination of *in vitro* and *in vivo* optogenetic and 2p imaging experiments. This new line allows temporally and spatially precise photostimulation with reliable activity read-out via 2p calcium imaging. We show for the first time all-optical read/write with 2p optogenetics using solely transgenic expression and demonstrate the use of the Ai203 reporter line in visual activity monitoring, behavior, and circuit mapping. Ai203 will facilitate a wide array of opto-physiological experiments in the mammalian brain to causally relate neural activity patterns to perception, cognition, and action.

Results

We generated a novel transgenic reporter line using the TIGRE2.0 system which drives Cre-dependent co-expression of the potent, ultra-fast opsin, ChroME and the sensitive calcium indicator GCaMP7s (Daigle et al., 2018; Dana et al., 2019; Mardinly et al., 2018). We used the Kv2.1 soma-targeting (st) sequence to enrich opsin expression at the soma, as described previously (Baker et al., 2016; Daigle et al., 2018; Forli et al., 2018; Lim et al., 2000; Mardinly et al., 2018; Wu et al., 2013). To ensure co-expression of the calcium sensor and the opsin, we fused GCaMP7s directly to the opsin ('st-ChroME-GCaMP7s'), producing a soma-targeted calcium indicator (Y. Chen et al., 2020; Shemesh et al., 2020). The construct additionally includes a FLAG tag for antibody labeling in post-mortem tissue when necessary. We termed this line, TITL-st-ChroME-GCaMP7s-ICL- nls-mRuby3-IRES2-tTA2, Ai203 (Fig.1A, see supplementary note).

To test this new transgenic line, we crossed it to the forebrain excitatory neuron driver, Slc17a7-IRES2-Cre (henceforth referred to as 'Vglut1-Cre') (Harris et al., 2014). Heterozygous double transgenic Vglut1-Cre;Ai203 mice exhibited high levels of st-ChroME-GCaMP7s expression across the entire forebrain (Fig. 1B-G, Fig. 1-Supplement 1). As expected, GCaMP7s appeared to be largely restricted to the membrane of the soma and proximal dendrites, similar to other st-ChroME preps (Fig. 1H, Fig. 1-Supplement 1). As has been noted for some other combinations of Cre-driver and TIGRE2.0 reporter lines, the TRE-dependent st-ChroME-GCaMP7s was sparsely expressed even though Vglut1-IRES2-Cre labels nearly all forebrain excitatory cells (Daigle et al., 2018; Harris et al., 2014). In contrast, the CAG-driven nls-mRuby3 was densely expressed, consistent with it labeling large fraction of Cre+ glutamatergic cells (Fig. 1J, Fig. 1-Supplement 1; supplementary note). Quantification of expression in primary visual cortex (V1) showed that 35 ± 6% of mRuby3+ cells were GCaMP7s+ (n=3 mice).

To examine Ai203 expression in other neural populations, we crossed Ai203 mice with Vgat-IRES-Cre mice to label all GABAergic neurons (Vong et al., 2011). We observed brain-wide expression in inhibitory neurons. In the cortex, GCaMP expression appeared weaker in Vgat-Cre;Ai203 mice than in Vglut1-Cre;Ai203 mice but was strong in the striatum and cerebellum (Fig. 1-Supplement 2).

Photostimulation and calcium imaging in Ai203 mice *in vitro*

A key test of this new line is whether st-ChroME-GCaMP7s is expressed at sufficient levels for both photostimulation and calcium imaging under a variety of conditions. Under conventional 1p illumination, we observed strong photocurrents with peak amplitudes of 3.4 ± 0.4 nA when measured in voltage clamp at -70 mV (Fig. 2A, n=13 cells). Using 2p illumination (via 3D Scanless Holographic Optogenetics with Temporal focusing (3D-SHOT), see Pegard et al., 2017 and Mardinly et al., 2018 for details) peak photocurrents were 1.7 ± 0.2 nA, comparable to that previously reported for viral ChroME (Fig. 2B; n=11 cells) (Mardinly et al., 2018). To test if these 2p-induced photocurrents were sufficient to evoke spiking, we made cell-attached recordings and illuminated the cells with trains of ten 5 ms light pulses at varying frequencies. Indeed, this reliably drove spiking at high frequencies (60 Hz) and low powers (13.5 mW) (Fig. 2C; n=11 cells). Neurons followed pulse trains with sub-millisecond jitter (0.86 ± 0.04 ms; n=11 cells) across all stimulation frequencies tested. These data demonstrate that Ai203 mice provide robust expression of soma-targeted ChroME that drives temporally precise, high fidelity spiking with both 1p and 2p activation.

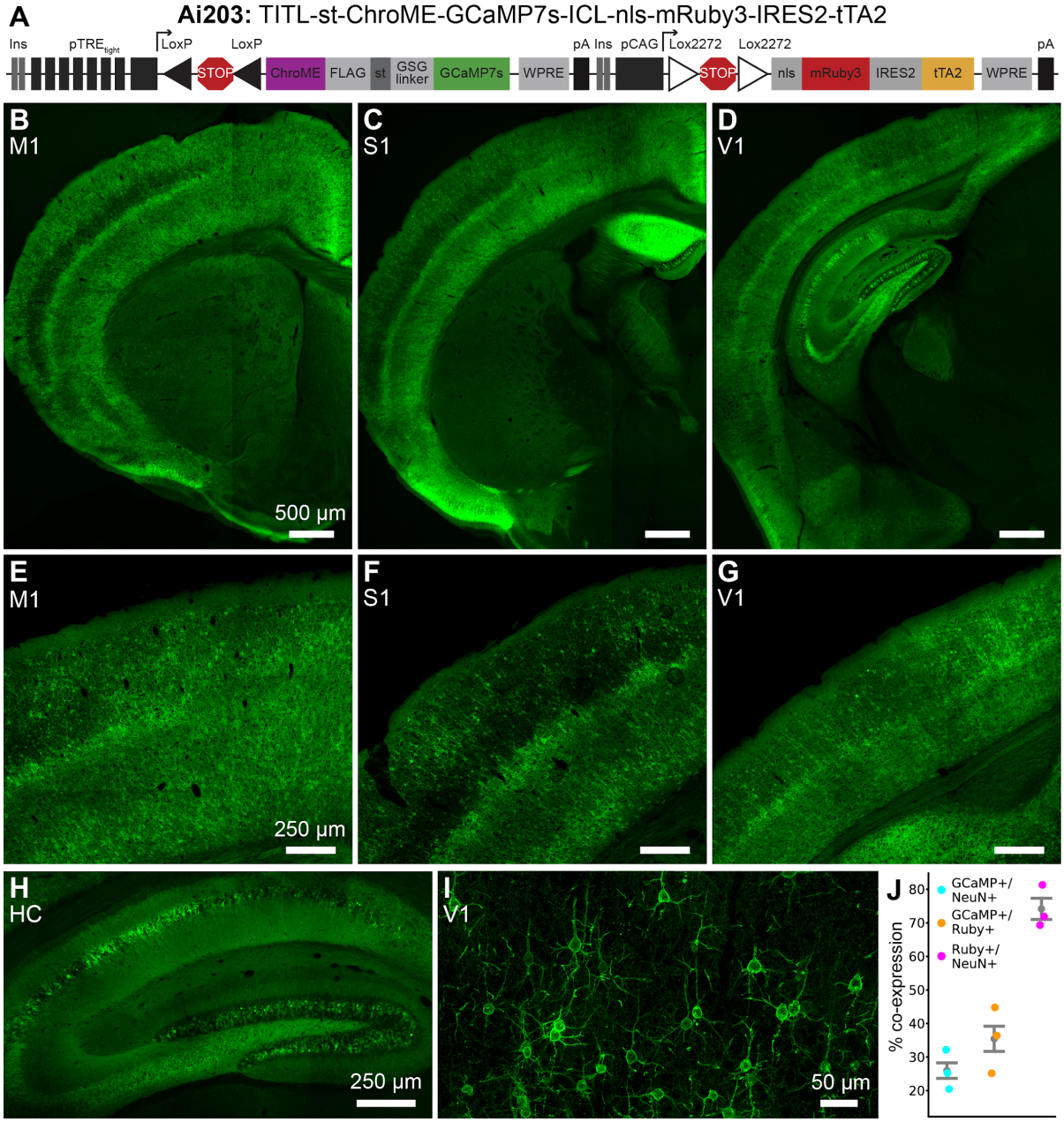

Figure 1: Vglut1-Cre;Ai203 mice have brain-wide expression of st-ChroME-GCaMP7s.
A: Schematic showing the Ai203 transgene.
B-H: Confocal images of a representative Vglut1-Cre/wt;Ai203/wt heterozygous double transgenic mouse showing GCaMP7s (green) expression in sections containing different brain regions (images stitched from multiple fields of view). M1: primary motor cortex; S1: primary somatosensory cortex; V1: primary visual cortex; HC: hippocampus
I: High-resolution maximum z-projection of neurons in V1.
J: Quantification of co-expression of GCaMP7s, anti-NeuN and mRuby3 based on manual cell counting in visual cortex (n=3 mice). Data are presented as mean ± bootstrapped 68% confidence interval.

Next, we tested whether the opsin-fused and soma-targeted GCaMP7s sensor is capable of sensitively reporting neuronal activity. We made whole-cell current clamp recordings from st-ChroME-GCaMP7s+ L2/3 neurons in brain slices, and induced spiking with short (5 ms) current injections through the patch pipette while measuring GCaMP7s fluorescence using 2p calcium imaging. We observed robust fluorescence responses for even small numbers of action potentials (Fig. 2D-E). Peak ΔF/F was 0.9 ± 0.1 for 10 action potentials (Fig. 2E, n=10 cells). Half-decay time for 10 action potentials was 1,350 ± 190 ms (Fig. 2F, n=9 cells), similar to that reported for cytosolic GCaMP7s (1,690 ± 60 ms decay, (Dana et al., 2019).

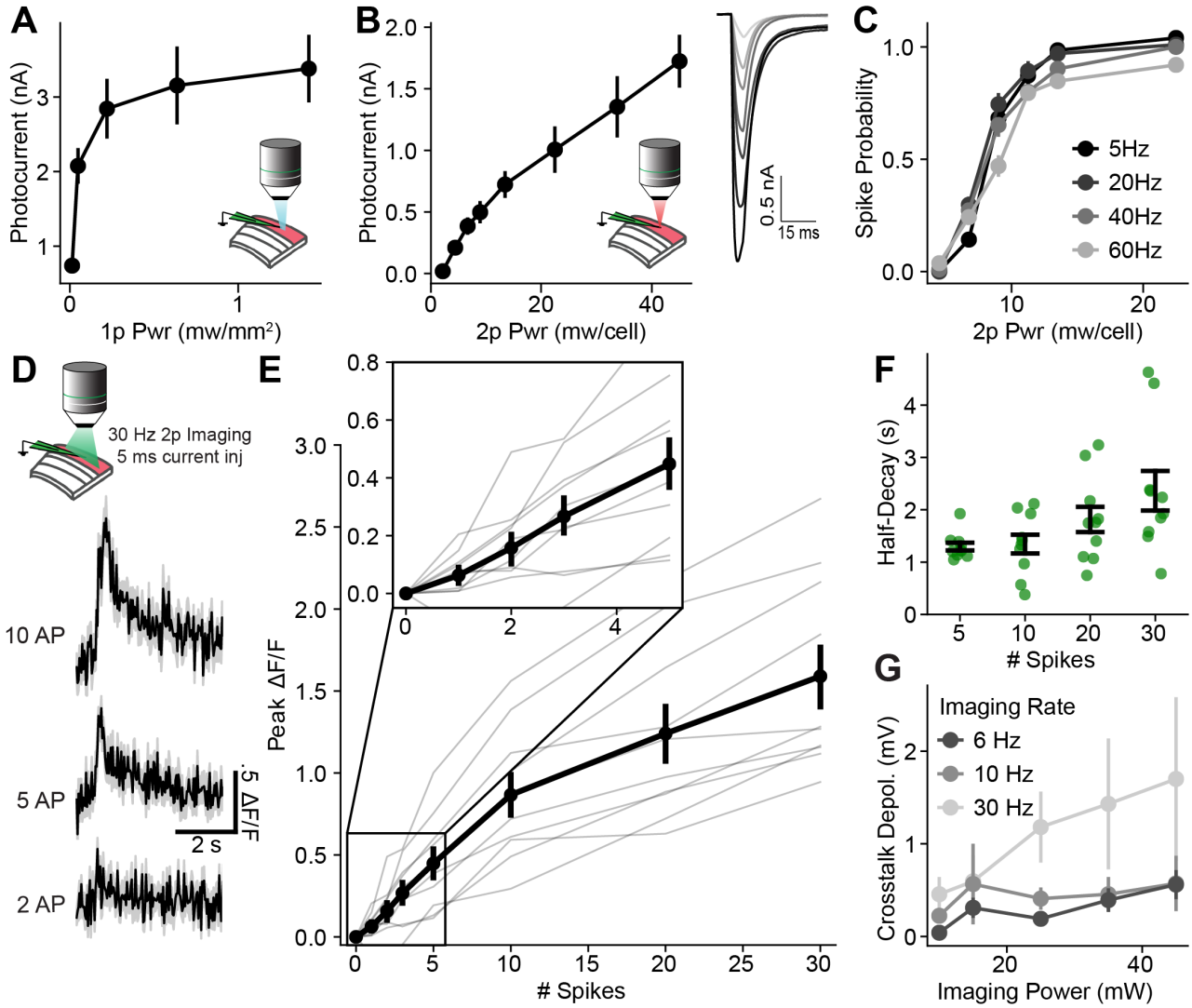

Figure 2: Strong photocurrents and GCaMP fluorescence responses in pyramidal cells expressing Ai203.
A: Photocurrents in opsin-positive L2/3 cells evoked by 1p illumination at 510 nm at varying powers. n=13 cells.
B: Left, same as (A) but for 2p illumination. Right, averaged evoked photocurrent traces for an example cell, power increases from light to dark. n=11 cells
C: Spike probability during 2p stimulation with a train of ten 5 ms pulses at different frequencies as a function of power. n=11 cells
D: Top, schematic and example image of GCaMP measurement experiments. Simultaneous whole cell recording and 2p imaging was conducted and cells were electrically stimulated with trains of 5 ms current injections at 30 Hz.
E: Peak ΔF/F fluorescence responses to different numbers of induced action potentials. Grey lines, individual cells. Black, average. Inset, closer view of responses for 1-5 spikes. n=10 cells.
F: Half-decay time in seconds for GCaMP7s responses, calculated from splined data. n=9 cells.
G: Mean depolarization induced by imaging laser when imaging at different frequencies with FOV size 980 x 980 µm and dwell time 46 ns/µm. n=4 cells.
A-C,G: data are presented as mean ± sem. E-F: data are presented as mean ± bootstrapped 68% confidence interval

146 In all-optical read/write experiments, the imaging laser can cause unintended activation of the opsin, a
147 phenomenon termed imaging "crosstalk" (Mardinly et al., 2018; Marshel et al., 2019; Packer et al., 2015).
148 To quantify crosstalk in Vglut1-Cre;Ai203 we made whole-cell current clamp recordings and recorded
149 voltage changes induced by 2p imaging. Under conditions commonly used for volumetric imaging in all-
150 optical experiments (FOV 980 × 980 µm, imaging rate 6-10 Hz, 46 ns/µm dwell time), mean depolarization
151 caused by the imaging laser was <1 mV (Fig. 2G, Fig2 – Figure Supplement 1, n=4 cells). These
152 experiments show that the st-ChroME-GCaMP7s fusion is compatible with imaging and produces strong
153 fluorescence responses with similar kinetics to cytosolic GCaMP7s.
154
155 **All optical interrogation of neural circuits with Ai203 mice *in vivo***
156 To determine whether the expression of st-GCaMP7s in Ai203 mice is sufficient to report sensory evoked
157 neural activity, we imaged calcium responses of L2/3 neurons in V1 through a cranial window (Fig. 3A)
158 (Andermann et al., 2013; Goldey et al., 2014). We observed robust st-GCaMP7s responses even at modest
159 2p imaging powers (~50 mW at 920 nm). Cells expressing st-GCaMP7s exhibited strong responses to high
160 contrast drifting gratings (Fig. 3B). Compared to another transgenic mouse line which expresses
161 cytoplasmic GCaMP6s (using Camk2a-tTA;tetO-GCaMP6s) and which were intracranially injected with an
162 AAV encoding ChroME, similar proportions of L2/3 cells were visually responsive (percent visually
163 responsive: Ai203, 39.6 ± 2.6%, n = 8 FOVs; Camk2a, 40.4 ± 2.4%, n = 12 FOVs, p=0.832, t-test) and
164 orientation tuned (percent orientation tuned: Ai203, 27.9 ± 1.3%, n = 5 FOVs; Camk2a, 33.3 ± 2.1%, n=8
165 FOVs, p=0.095, t-test, Fig. 3C). Orientation-selective responses were similar, though orientation selectivity
166 index (OSI) across the population of orientation tuned cells was slightly lower (OSI: Ai203, 0.56 ± 0.04, n =
167 8 FOVs; Camk2a, 0.66 ± 0.01, n = 5 FOVs, p=0.0167, t-test; Fig. 3D). Despite this minor difference, we
168 were able to measure orientation tuning across many neurons, demonstrating that the Ai203 reporter line is
169 suitable for large scale calcium imaging of sensory evoked neural responses *in vivo*.
170
171 A primary use for the combined expression of st-ChroME and GCaMP7s is *in vivo* targeted optogenetic
172 manipulation using multiphoton optogenetics. To validate the utility of Ai203 with 2p optogenetics *in vivo*,
173 we used 3D-SHOT to holographically illuminate neurons and ensembles of neurons while simultaneously
174 imaging st-GCaMP7s responses using conventional multiplane 2p imaging. 2p photostimulation
175 consistently drove large increases in st-GCaMP7s fluorescence in targeted cells (Fig. 3D-E, Video 1).
176 Compared to mice intracranially injected with an AAV encoding st-ChroME (same mice as used above),
177 Ai203 mice had a higher percentage of ChroME+ cells activated at all powers tested (proportion activated:
178 Ai203, n=7; Virus, n=12, p=0.00012, 2-way repeated measures ANOVA, Fig. 3F). This high sensitivity
179 enabled the co-activation of large ensembles of neurons with a single hologram, which we demonstrated by
180 illuminating 49 L2/3 neurons simultaneously (Fig. 3G-H). Even during this large ensemble stimulation,
181 neighboring non-targeted cells showed minimal activation, demonstrating that the Ai203 reporter is suitable
182 for large-scale, high resolution photostimulation (Fig. 3H).

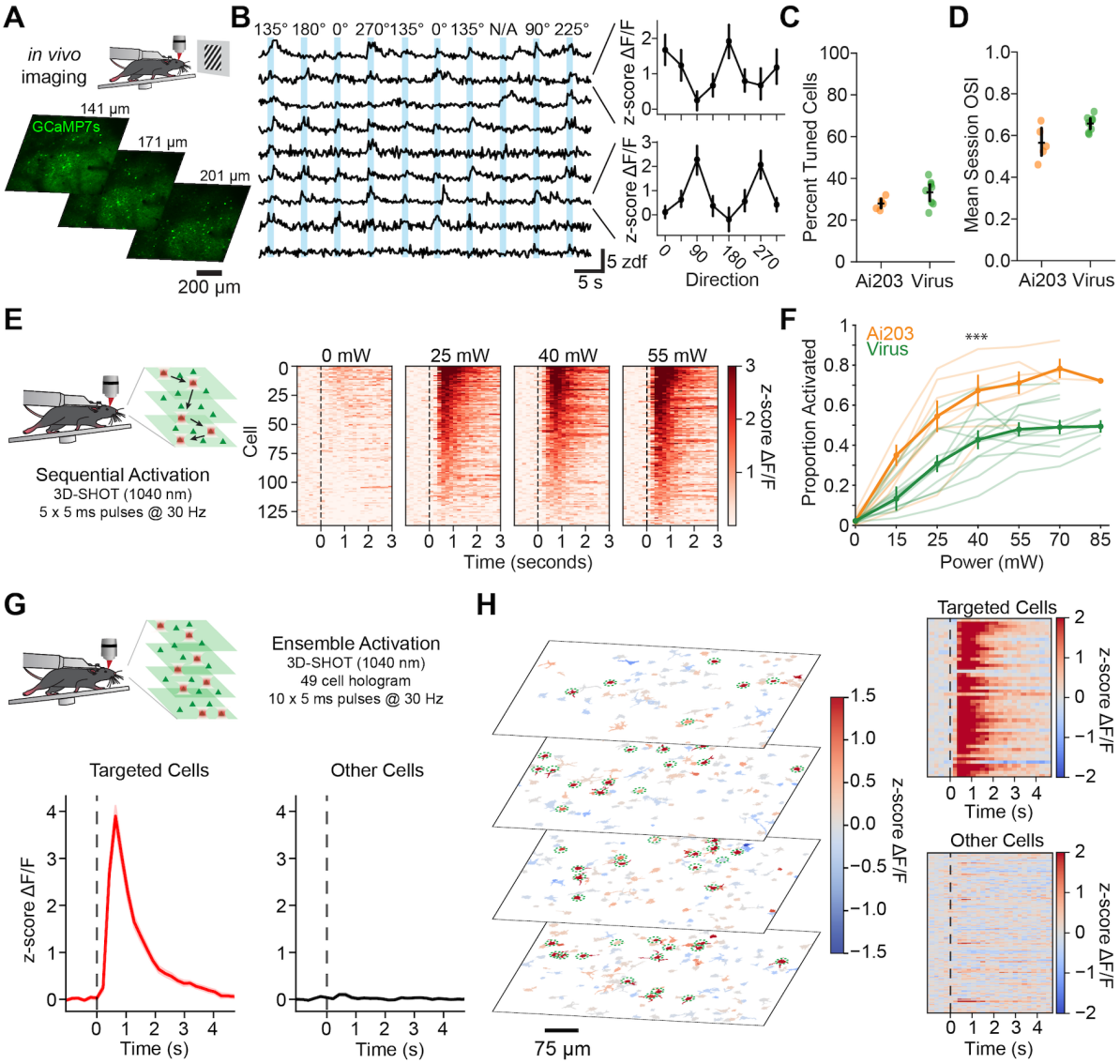

Figure 3: 2p imaging of *in vivo* visually- and holographically-evoked responses in Vglut1-Cre;Ai203 mice

A: Top, schematic of in vivo imaging paradigm. Bottom, example fields of view for 3-plane (6.36 Hz volumetric) imaging.

B: Left, example traces of fluorescence responses to drifting gratings in V1 pyramidal cells expressing st-ChroME-GCaMP7s. Right, direction tuning curves for 2 example cells. Scale bar applies to all example calcium traces.

C: Comparison of percent significantly tuned cells in Vglut1-Cre;Ai203 mice (orange, n=5 FOVs) and Camk2a-tTA;tetO-GCaMP6s mice expressing viral st-ChroME (green, n=8 FOVs). Mice expressing ChroME transgenically and virally had similar numbers of visually responsive, tuned cells (p= 0.095, t-test).

D: Comparison of mean orientation selectivity index (OSI) per session of significantly orientation-tuned cells, averaged by session for Vglut1-Cre;Ai203 mice (green) compared to Camk2a-tTA;tetO-GCaMP6s mice (p = 0.016).

E: Left, schematic of single-cell holographic stimulation experiment. Targeted cells were sequentially activated across 3 z-planes. Right, heatmaps of z-scored ΔF/F responses at different powers for 110 significantly activated cells in an example session (16, 84, 82, and 110 cells were activated at 0, 25, 40, and 55 mW, respectively. one-tailed, rank sum test).

F: Quantification of fraction of neurons activated at various stimulation powers during single-cell stimulation (p = 0.00012, repeated measures ANOVA).

G: Schematic of ensemble stimulation experiment and average responses from targeted (left, red) and other non-targeted (black, right) cells. 49 neurons across 4 z-planes were activated simultaneously.

H: Left, images showing individual cell responses during stimulation of 49 cells in a single hologram. Cell masks are colored by z-scored ΔF/F. Right, heatmap showing individual cells z-scored ΔF/F for targeted cells (49 cells, top) and all other cells (445 cells, bottom). 46/49 cells were significantly activated by stimulation (p<.05, one-tailed rank sum test).

Data are presented as mean ± sem.

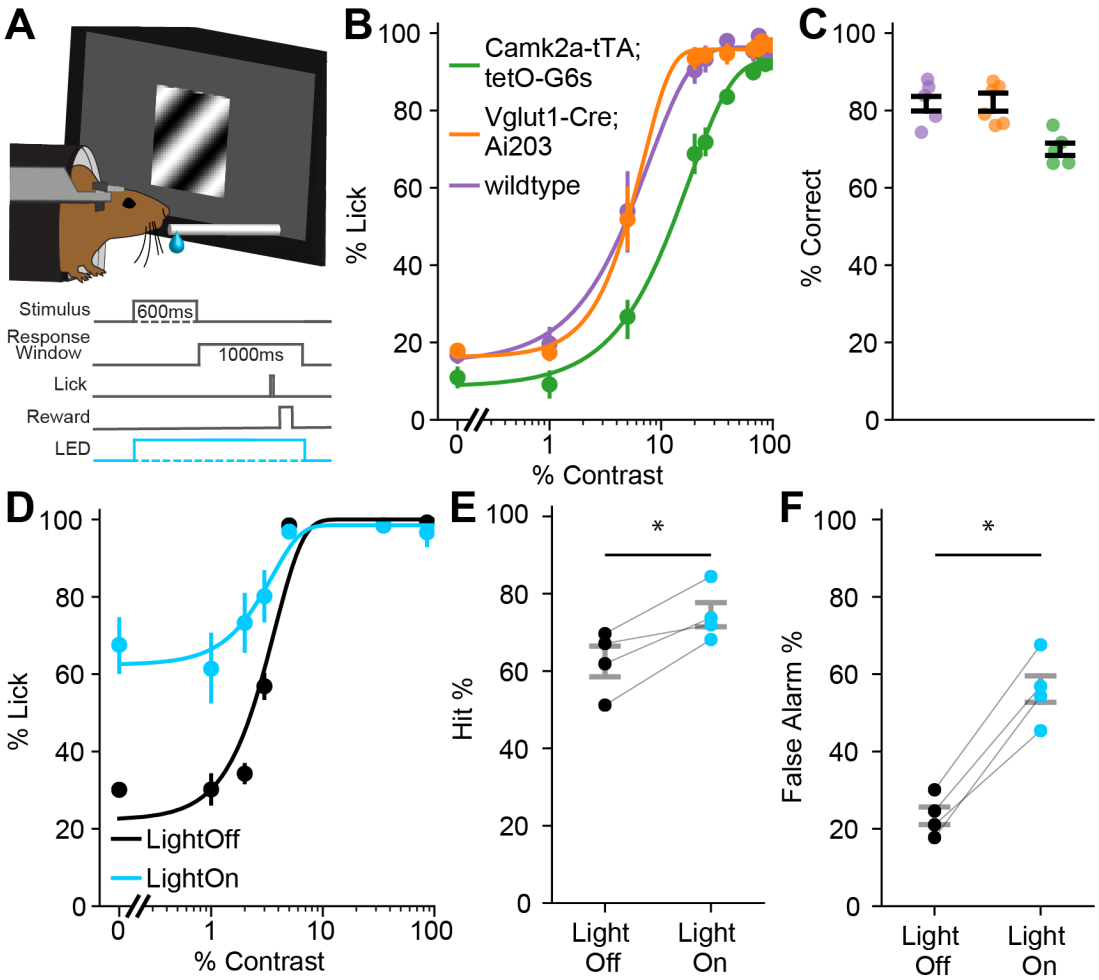

Figure 4: Optogenetic manipulation of operant behavior Vglut1-Cre;Ai203 mice alters performance
A: Schematic of the visual detection task. Gratings of varying contrasts were presented to mice trained to lick during a 1 second response window following stimulus presentation to indicate detection.
B: Psychometric curves averaged across mice for of the three strains tested. n=6 mice for Vglut1-Cre;Ai203, n=5 each for wildtype and Camk2a-tTA;teto-GCaMP6s.
C: Comparison of % correct, points are individual mice. % correct across genotypes: one-way ANOVA p=0.0025 with post-hoc Tukey test: Ai203 vs wildtype p=0.90; Ai203 vs tetO p=0.0050; tetO vs wildtype p=0.0056.
D: Psychometric curves averaged across four sessions from one example mouse showing behavioral change with 1p stimulation at 470 nm of V1 excitatory cells.
E-F: Comparison of performance metrics with and without 1p stimulation. Hit (E) and False Alarm (F) rates significantly increased (hit rate: p=0.019, false alarm rate: p=0.0016, paired t-test, n=4 mice) with photostimulation of excitatory cells. Points are individual mice, average of four sessions per mouse.
Data are presented as mean ± bootstrapped 68% confidence interval.

Measuring and manipulating visual behavior in Ai203 mice

Transgenic opsin and GCaMP expression is particularly advantageous in behavioral training paradigms where long-term stability is essential. To test whether Vglut1-Cre;Ai203 mice are generally suitable for operant behavior, we trained them on a visual contrast detection task (Fig. 4A). Similar detection tasks are known to be V1-dependent (Cone et al., 2020; Glickfeld et al., 2013; Ruediger & Scanziani, 2020). Vglut1-Cre;Ai203 mice readily learned the task: 9 of 10 trained Vglut1-Cre;Ai203 reached the performance criteria (>90% hit, <30% false alarm), in a median of 9 training days. To confirm that mice could not only learn the task, but perform at high levels, we compared performance to wildtype (wt) mice and Camk2a-tTA;tetO-GCaMP6s mice. Vglut1-Cre;Ai203 mice performed as well as or better than the other strains (Fig. 4B-C). Camk2a-tTA;tetO-GCaMP6s had a lower % correct than Vglut1-Cre;Ai203, but Vglut1-Cre;Ai203 was indistinguishable from wildtype (Fig. 4C; % correct across genotypes: one-way ANOVA p=0.0025 with post-hoc Tukey test: Ai203 vs wt p=0.90; Ai203 vs Camk2a p=0.0050; Camk2a vs wt p=0.0054; n=16

mice, n=6 mice for AI203, n=5 mice for wt and Camk2a). Thus, Vglut1-Ai203 mice learn and perform this visual detection task comparable to wildtype mice, implying that transgene expression does not negatively alter behavioral performance.

We next asked if optogenetic stimulation in Vglut1-Cre;Ai203 mice could alter behavioral performance on this visual contrast detection task. Indeed, photostimulation via a 470 nm optic fiber over V1 through a cranial window induced a dramatic increase in the false alarm rate and the hit rate for weak stimuli (Fig. 4D-F; Hit rate: no light 62 ± 4%, light 75 ± 3%, p=0.019; False alarm rate: no light 23 ± 3%, light 56 ± 5%, p=0.0016; paired t-test; n=4 mice). Similar results were observed from activation of excitatory neurons in V1 in other studies (Cone et al., 2020; Jin & Glickfeld, 2019). Thus, Vglut1-Cre;Ai203 mice can be used for probing the impact of cell-type specific optogenetic manipulations on behavior.

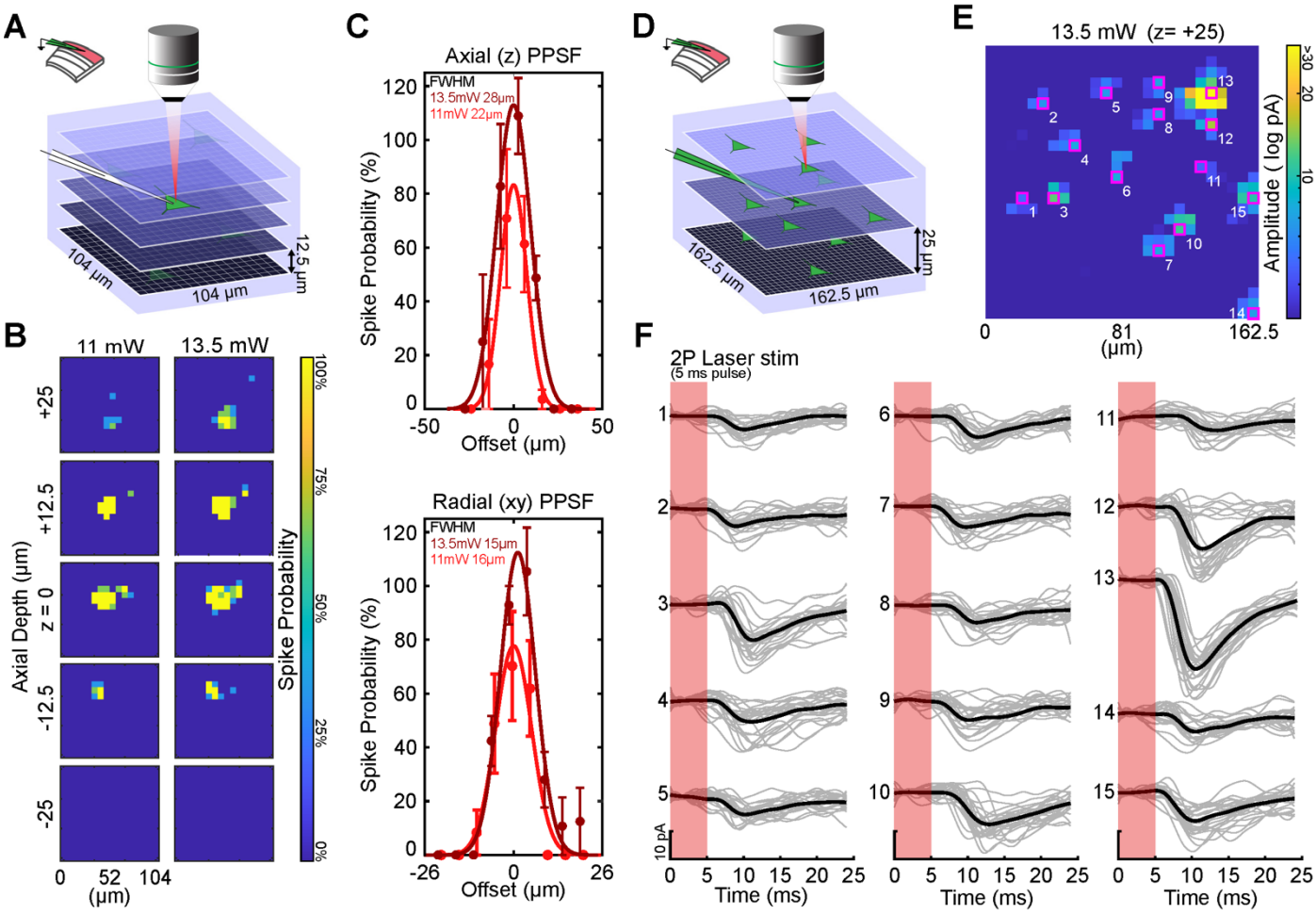

Figure 5: High resolution 2p holographic synaptic connectivity mapping in Ai203 mice.
A) Schematic of protocol for assessing spatial resolution with 3D holographic stimulation.
B) Heatmaps from an example opsin-positive cell depicting spike probability across five planes and two laser powers. Depth z = 0 corresponds to the plane of the patched cell.
C) Physiological point-spread function (PPSF) of photostimulation-evoked spiking of opsin-positive neurons measured by loose-patch recordings (axial at top and radial at bottom). n=4 cells.
D) Schematic of protocol for "all-to-one" mapping of synaptic connectivity. 2p holograms were rapidly projected onto a 3D grid (162.5 × 162.5 × 100 µm) at 6.5 × 6.5 × 25 µm spacing (3380 total voxels) while an opsin-negative cell in the middle of the grid (*z* = 0) was voltage clamped to measure postsynaptic excitatory synaptic currents.
E) Example heatmap of evoked postsynaptic EPSC amplitude by xy location of photostimulation sites in a plane z = 25 µm above the patched cell. The pixels with the highest average EPSC amplitude (across 20 trials) in 15 pixel clusters are highlighted in magenta.
F) The photostimulation evoked postsynaptic responses (gray) and their average (black) from the 15 pixels selected in E.
Data are presented as mean ± sem.

256 **2p Synaptic Connectivity Mapping**

257 Finally, we tested the use of Ai203 in *in vitro* synaptic connectivity mapping by using 2p optogenetics to
258 rapidly identify putative monosynaptic connections to a neuron of interest (Baker et al., 2016; Hage et al.,
259 2019; Karnani, Jackson, Ayzenshtat, Sichani, et al., 2016; Karnani, Jackson, Ayzenshtat, Tucciarone, et al.,
260 2016; Naka et al., 2019; Packer et al., 2012; Shemesh et al., 2017). We first measured the effective spatial
261 resolution of photostimulation by recording spiking in an opsin-positive L2/3 pyramidal neuron while
262 stimulating each point in a smaller 3D grid surrounding the cell (Fig. 5A). We found an effective spatial
263 resolution on par with previous reports using 3D-SHOT with soma-targeted opsins (Fig. 5A-C; FWHM @
264 13.5 mW = 15 ± 2 μm radial; 28 ± 4 μm axial) (Mardinly et al., 2018; Pégard et al., 2017). To activate and
265 identify putative presynaptic inputs, we stimulated individual spots in a larger 3D grid (Fig. 5D) while
266 performing whole-cell voltage clamp recordings from an opsin-negative L2/3 pyramidal cell. We
267 consistently identified between 11-15 putative monosynaptic connections to the patched cell within a single
268 plane (Fig. 5E, Fig. 5 – Supplement 1). These data demonstrate that 2p holographic optogenetics applied to
269 the Vglut1-Cre;Ai203 transgenic line is suitable for mapping intracortical excitatory synaptic connectivity
270 rapidly and volumetrically across brain tissue.
271

272 **Discussion**

273 We developed and validated the first Cre-dependent reporter line that enables all-optical
274 interrogation of neural circuits with high spatial and temporal precision with 2p imaging and 2p holographic
275 optogenetics. The Ai203 is a multifunctional reporter line co-expressing both an ultrapotent opsin, ChroME,
276 and a high-performance calcium indicator, GCaMP7s, as a single soma-targeted fusion protein: st-ChroME-
277 GCaMP7s. Although Cre reporter lines for opsins or calcium sensors exist, none are soma-targeted and none
278 co-express both an opsin and a calcium sensor. Because the Ai203 transgenic line obviates the need for one
279 or more viruses to co-express the opsin and the calcium indicator it will facilitate a variety of all-optical
280 experiments by providing more reliable, reproducible, and stable transgene expression. Critically, transgenic
281 expression of st-ChroME-GCaMP7s in Vglut1-Cre;Ai203 did not compromise cell, circuit, or behavioral
282 function by any assay we tested.

283 The high levels of ChroME expression in Vglut-1;Ai203 mice allowed us to photostimulate opsin-
284 expressing neurons with even lower laser powers than mice injected with virally expressed ChroME. Taking
285 advantage of this strong and stable expression we demonstrated simultaneous activation of an arbitrary,
286 experimenter-designated combination of nearly 50 neurons simultaneously *in vivo*, a number that exceeds
287 what is sufficient to induce behavioral changes (Carrillo-Reid et al., 2019; Daie et al., 2021; Dalgleish et al.,
288 2020; Gill et al., 2020; Marshel et al., 2019). Thus, the Ai203 line should be useful for probing causal
289 relationships between ensemble activity and behavior.

290 Mapping synaptic connectivity between different cell types is a critical means by which one can
291 relate the structure of neural circuits to their function. Here we demonstrated that the Ai203 reporter line can
292 be used to rapidly map synaptic connectivity by recording postsynaptic currents while performing 2p
293 stimulation. Prior 2p mapping experiments used either viral tools that result in opsin expression variability
294 within and across animals, or transgenic lines that do not have soma-targeted expression of opsins (Baker et
295 al., 2016; Hage et al., 2019; Karnani, Jackson, Ayzenshtat, Sichani, et al., 2016; Karnani, Jackson,
296 Ayzenshtat, Tucciarone, et al., 2016; Naka et al., 2019; Packer et al., 2012; Shemesh et al., 2017). The
297 Ai203 reporter line combines the advantages of soma-targeting with the convenience of transgenic
298 expression. The widespread transgenic expression of st-ChroME will be particularly advantageous for long
299 range connectivity mapping. In future experiments, the reliable co-expression of ChroME and GCaMP7s

can be used to confirm spiking in opsin-positive presynaptic cells, which aids the interpretation of synaptic mapping experiments (Baker et al., 2016).

While Ai203 is particularly advantageous for 2p optogenetics, the potent st-ChroME expression will also assist in applications involving conventional 1p activation. As one example, we demonstrated that 1p activation of V1 in Vglut1-Cre;Ai203 mice altered performance in a detection task, matching previous findings using channelrhodopsin in excitatory neurons (Cone et al., 2020; Jin & Glickfeld, 2019). In addition, soma-targeting is important for less conventional 1p approaches where spatial resolution with 1p illumination is needed (Wu et al., 2013; Xue et al., 2020).

One important issue to consider with this reporter line is the incomplete coverage transgene expression in Cre+ cells. We found that when using the pan-excitatory driver Vglut1-IRES2-Cre (Harris et al., 2014), only about 35% of cortical excitatory neurons expressed the transgene. Other combinations of Cre driver and TIGRE1.0 and 2.0 reporter lines have shown this sparsity, which is thought to be due in part to promoter silencing of TRE (see supplementary note for further discussion) (Daigle et al., 2018; Madisen et al., 2015). While sparse labeling precludes all-optical control and readout from many Cre+ neurons, it also offers advantages in many 2p optogenetic experiments (both in vivo and ex-vivo) due to reduced activation of neighboring cells (Adesnik & Abdeladim, 2021). Use of layer-specific driver lines, such as Cux2-Cre, has been observed to produce dense labelling in other TIGRE lines, perhaps due to lower overall expression improving animal health, and may provide more complete coverage. Further testing of different crosses, including in other cell types, will be beneficial to examine if denser expression is possible.

The soma-targeted GCaMP construct here was produced by fusing GCaMP7s with an opsin that is soma-targeted via the Kv2.1 sequence. We observed robust fluorescence changes with GCaMP7s in response to small numbers of action potentials and reliably observed sensory-evoked activity *in vivo*. Previous work with soma-targeted GCaMPs have shown that they reduce neuropil contamination, a common issue with both 1p and 2p calcium imaging (Y. Chen et al., 2020; Shemesh et al., 2020). The soma targeting of GCaMP7s in the Ai203 line should likewise reduce contamination by signals from the neuropil. However, Ai203 mice should not be used with conventional 1p imaging since the illumination light for GCaMP7s will activate the ChroME opsin, causing substantial depolarization. Instead, Ai203 mice are well-suited for use with 2p laser scanning microscopy, and we found minimal optical crosstalk of the opsin by the 2p scanning laser under conventional imaging conditions.

This novel multifunctional reporter line will facilitate a wide variety of optogenetic and optogenetic/imaging experiments for interrogating neural circuits and relating neural activity patterns to behavior. More reliable and stable expression of the opsin and the calcium sensor in the Ai203 line compared to viral approaches will make such experiments more reproducible between animals and between studies. The convenience of co-expressed opsin and calcium sensor will substantially facilitate challenging all-optical experiments for probing behavior in trained mice. The soma-targeting of both the opsin and the calcium sensor will improve resolution of read/write compared to existing strains, and strong, stable expression of the ultrapotent opsin ChroME will be useful for a variety of applications, such as large-scale ensemble stimulation. Our results demonstrate that Ai203 mice can become a highly valuable tool in the neuroscientist's toolbox.

Acknowledgements

We thank the members of the Adesnik lab for comments, Savitha Sridharan for advice on construct development, Janine Beyer for technical support, and Nikhil Bhatla for assistance with histology. Hillel Adesnik is a New York Stem Cell Robertston Investigator. This work was supported by the New York Stem

Cell Foundation, National Institutes of Health (NIH) Grant UF1- NS107574 (H.A.), NIH Grant U19-NS107613 (H.A.), NIH Grant RF1- RF1MH120680 (H.A.), NIH Grant RO1- EY023756 (H.A.), National Science Foundation Graduate Research Fellowship (DGE 1752814 (H.A.B.)), NIH Grant F31-EY031977 (W.D.H.), NIH Grant K99-EY029758 (I.A.O.), NIH Grant U19-MH114830 (H.Z.). The content is solely the responsibility of the authors and does not necessarily represent the official views of the National Institutes of Health or the National Science Foundation.

350

351 **Supplementary note on expression:**

352 In the TIGRE2.0 system, two separate transgene-expressing units are co-inserted into the TIGRE locus
353 (Daigle et al., 2018). Both are Lox-Stop-Lox (LSL) controlled, but the first is TRE driven and the second is
354 CAG driven. In Ai203, the st-ChroME-GCaMP7s is TRE-driven, while the second CAG-driven unit
355 contains an nls-mRuby3 and the tTA2 that drives the first unit (full gene: TITL-st-ChroME-GCaMP7s-ICL-
356 nls-mRuby3-IRES2-tTA2; Fig. 1A).

357 Certain combinations of Cre-driver and TIGRE2.0 reporter lines drive expression of the TRE-driven protein
358 in only a subset of Cre+ cells, most notably in crosses containing Pvalb-Cre (Daigle et al., 2018). In other
359 TIGRE2.0 reporter lines with one TRE-driven fluorophore and one CAG-driven fluorophore, the CAG-
360 driven fluorophore has been expressed in almost all the target population even when the TRE-driven
361 fluorophore is sparsely expressed relative to the expected Cre+ population. This is thought to be due
362 primarily to promoter silencing of the TRE promoter, not due to a lack of tTA2. Consistent with this, the
363 CAG-driven nls-mRuby3 in Ai203 was densely expressed (74 ± 4% of all anti-NeuN labelled neurons),
364 while the TRE-driven st-ChroME-GCaMP7s was sparser.

365

366 This sparsity has not been noted in excitatory cortical cells before. Unlike previously published TIGRE2.0
367 lines, Ai203 has an IRES2-tTA2 and uses the TREtight rather than the TRE2 promoter. The IRES2 will
368 likely decrease expression of the tTA2, which may reduce overall expression levels, but could lead to
369 greater overall health. TREtight is more prone to silencing, so this may lead to the lower expression seen in
370 Ai203 compared to other TIGRE2.0 lines.

371

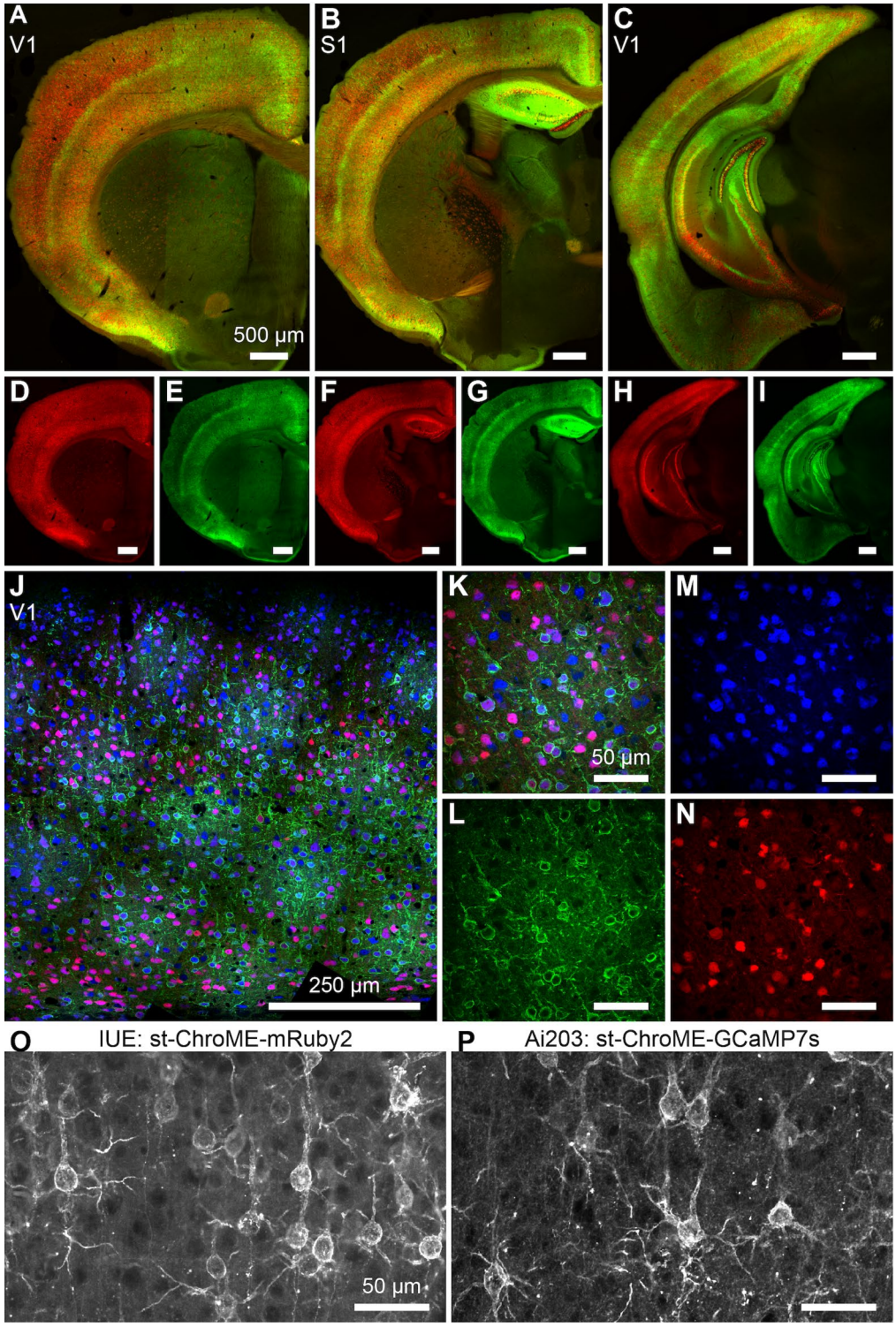

Figure 1 – Figure Supplement 1: Expression of nls-mRuby3 and GCaMP7s in Vglut1-Cre;Ai203

A-I: Confocal images of brain sections from Vglut1-Cre;Ai203 mice showing expression of st-ChroME-GCaMP7s (green) and nls-mRuby3 (red) (images stitched from multiple fields of view). A-C, composite images of both mRuby3 and st-ChroME-GCaMP7s. D-I, sections in A-C separated by channel

J: One of three areas used for quantification of expressing cells, showing in anti-NeuN (blue), nls-mRuby3 (red), st-ChroME-GCaMP7s (green). Area is composed of stitched fields of view taken at high magnification for good optical sectioning, then rotated and cropped to get a full depth section.

K-N: one example field of view from the area in J. K: composite, M: anti-NeuN, L: st-ChroME-GCaMP7s, N: nls-mRuby3

O-P: Comparison of in utero electroporation (IUE) st-ChroME-mRuby2 to transgenically expressed st-ChroME-GCaMP7s

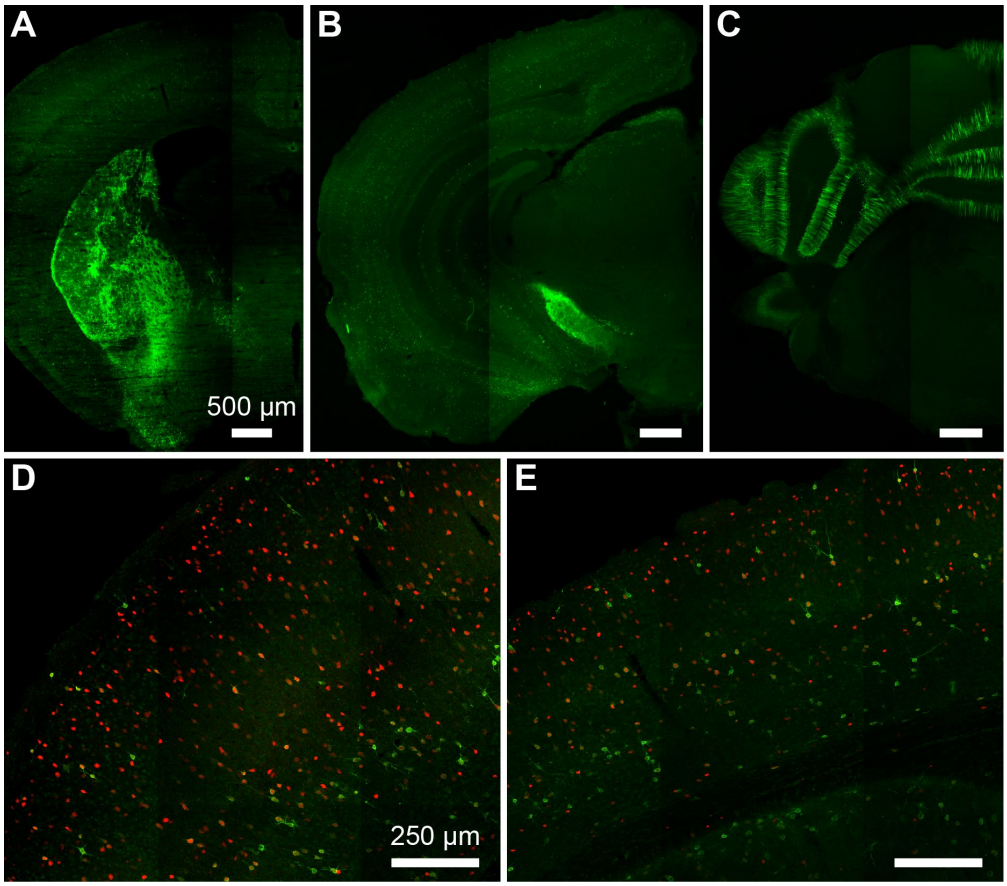

Figure 1 - Figure Supplement 2: Expression of GCaMP7s and nls-mRuby3 in Vgat-IRES2-Cre; Ai203 mice
A-C: Confocal images of post-mortem tissue from one example mouse at three different coronal sections showing st-ChroME-GCaMP7s expression in green (images stitched from multiple fields of view).
D-E: Expression of st-ChroME-GCaMP7s (green) and nls-mRuby3 (red) in S1 (D), V1 (E).

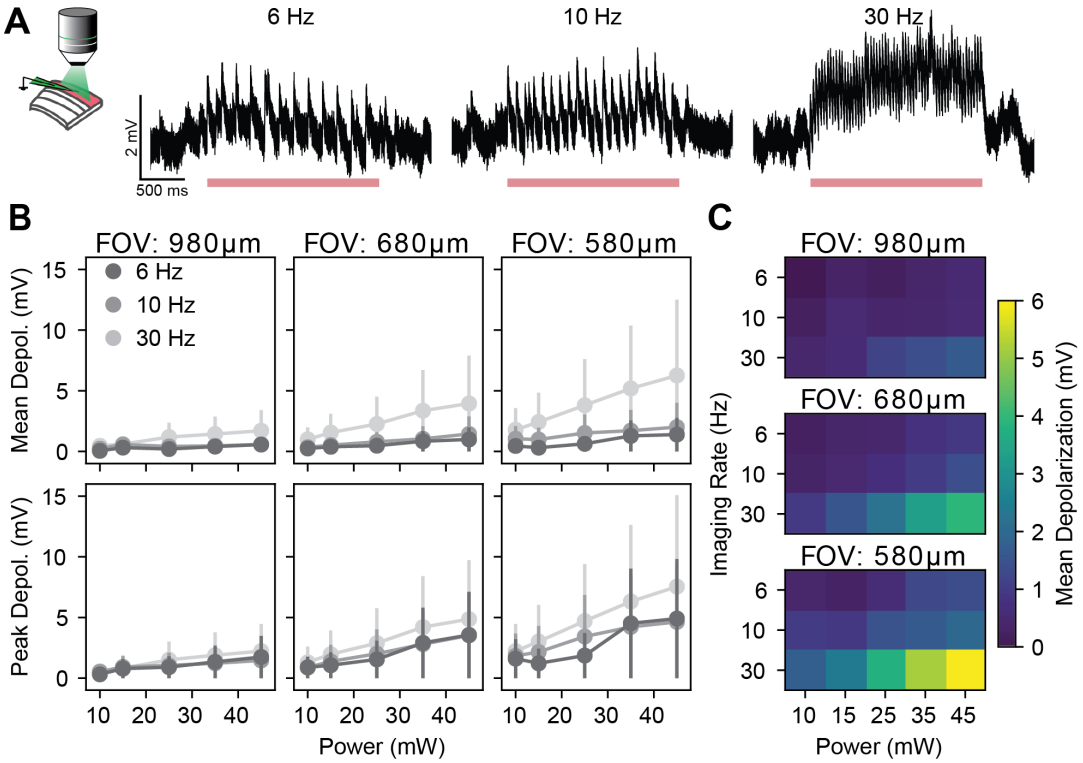

Figure 2 – Figure Supplement 1: 2p scanning-evoked depolarization *in vitro*.
A: Left schematic of experimental setup. Whole-cell recordings were made during 2p imaging with different imaging rates, powers, and scanning field of view (FOV) sizes. Scanning-induced depolarization, or "cross talk," was recorded. Right, 3 example traces from one cell recorded at different frequencies, all with 45 mW imaging power and a 980 µm FOV.
B: Mean (top) and peak (bottom) depolarization during 2p imaging of opsin-positive neurons. From left to right, increasing zoom and decreasing field of view size, and increasing dwell times (FOV 980: 46 ns/um; FOV 680: 66 ns/um; FOV 580: 78 ns/um). Data are shown as mean ± sem.
C : Same as in top of B, visualized as heatmaps.

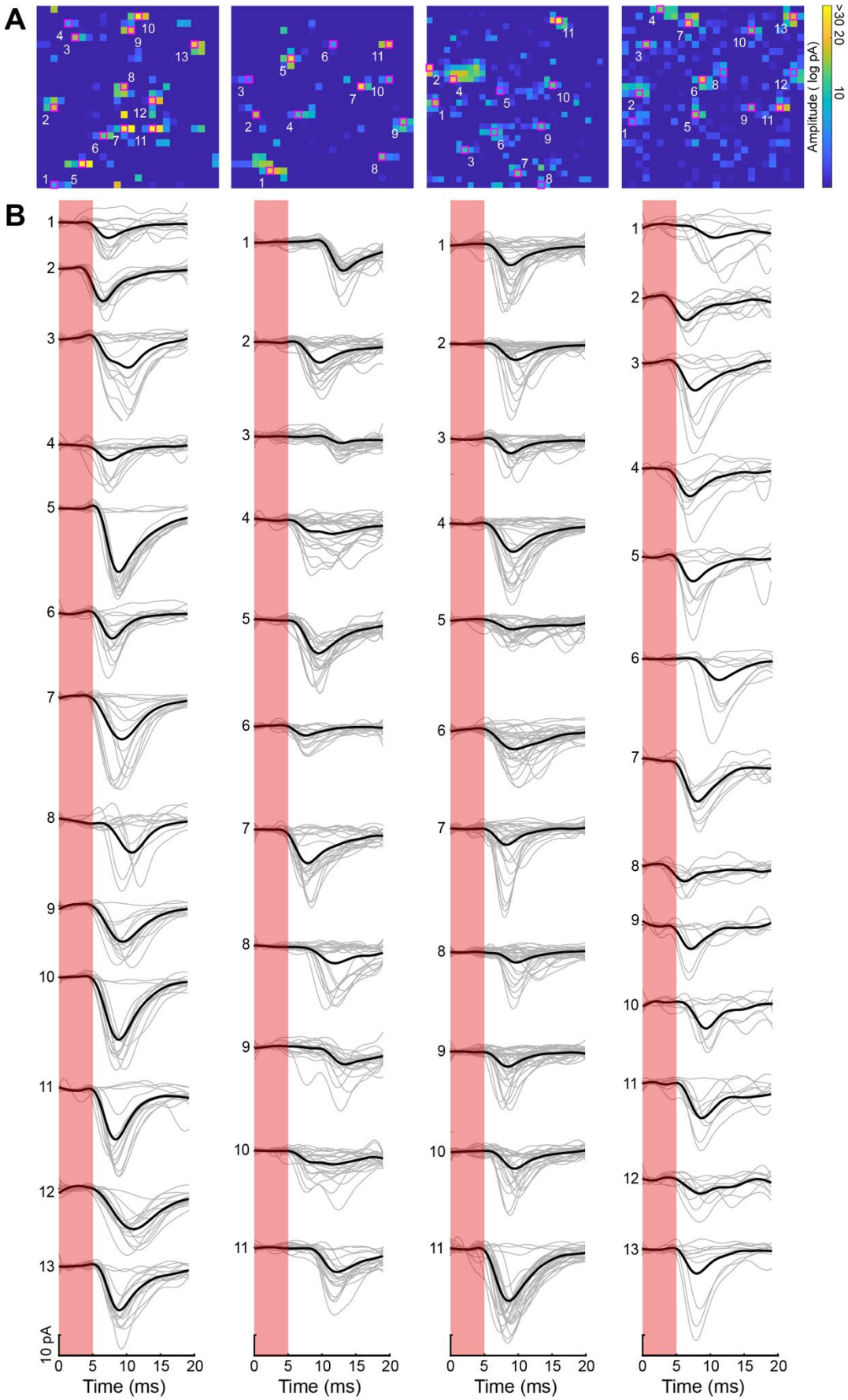

Figure 5 – Figure Supplement 1: Examples of high resolution 2p holographic synaptic connectivity mapping in Ai203 mice.
A: For four different example cells, heatmaps of evoked postsynaptic EPSC amplitude by xy location of photostimulation sites in single nearby z planes. The pixels with the highest average EPSC amplitude (across 20 trials) are highlighted in red.
B) The photostimulation-evoked postsynaptic responses (gray) and their average (black) from the pixels selected in A.

401 **Methods:**

402 **Mouse creation:**

403 The Ai203 transgenic mouse line was generated similarly as previously described (Daigle et al.,
404 2018; Madisen et al., 2015). The targeting vector was constructed using gene synthesis and standard
405 molecular cloning techniques. It contains the following components: FRT3 – 2X HS4 chicken beta globin
406 insulators – TREtight promoter – LoxP – ORF-3X stops – hGH polyA, PGK polyA – LoxP – ChroME-
407 FLAG-Kv2.1-GSGlinker-GcaMP7s– WPRE-bGH polyA – 2X HS4 chicken beta globin insulators – CAG
408 promoter – Lox2272 – ORF-3X stops – hGH polyA, TK polyA – Lox2272 – nls-mRuby3-IRES2-tTA2 –
409 WPRE – bGH polyA – PhiC31 attB- PGK promoter – Hygro1-SD – FRT5. Targeting of the transgene
410 cassette into the TIGRE locus was accomplished via Flp-recombinase mediated cassette exchange using
411 circularized targeting vector and a CAG-FlpE vector (Open Biosystems Inc) as previously described (Daigle
412 et al., 2018; Madisen et al., 2015). Correctly targeted ES cells were identified using PCR and injected into
413 blastocysts to obtain chimeras and subsequent germline transmission. Resulting mice were then crossed to
414 C57BL/6J mice and maintained in C57BL/6J congenic background. Only mice heterozygous for both
415 reporter and driver transgenes (Slc17a7-IRES2-Cre;Ai203) were used for experiments.
416

417 **Histology:**

418 Mice were anesthetized with ketamine and transcardially perfused with phosphate-buffered saline
419 (PBS) and then 4% paraformaldehyde (PFA). Brains were left in PFA overnight, then transferred to 30%
420 sucrose for 1-2 days, then cut into 40 μm-thick coronal sections using a freezing microtome and stored in
421 PBS until use.

422 For NeuN immunostaining, sections were blocked for 1 hour at 4 degrees on a rocker in PBS
423 containing 3% normal goat serum (NGS), 0.6% Triton X-100, 0.2% Tween-20, and 3% bovine serum
424 albumin (BSA). For primary staining, sections were incubated overnight at 4 degrees on a rocker in Rabbit
425 anti-NeuN (Abcam) diluted 1:10,000 in blocking solution. The next day, sections were washed once in PBS
426 with 0.25% Triton X-100 (PBS-T). For secondary staining, sections were incubated for one hour on the
427 rocker at room temperature in blocking solution with 1:1000 Goat anti-Rabbit IgG H&L Alexa Fluor 405
428 (Thermo Fisher Scientific). Then sections were washed once in PBS-T. Sections were mounted and
429 coverslipped with Vectashield (Vector Laboratories Inc).

430 Images were collected on an Olympus FV3000 (Olympus Corporation) confocal laser scanning
431 microscope. For cell counting, to obtain adequate z-sectioning, fields of view tiled at 212 × 212 μm (800 ×
432 800 pixels) each were taken spanning an area of V1, stitched in ImageJ with a stitching plugin (Preibisch et
433 al., 2009). Then images were rotated so that the pia was horizontal and cropped so that the counting area
434 was a rectangular column of cortex containing all layers, to evenly count all layers. Cells were counted in
435 ImageJ using built-in tools.

436 For comparison to in utero electroporated st-ChroME-mRuby3, in utero electroporation was
437 performed as described previously (Sridharan et al., 2021).
438

439 **Two-photon holographic microscopy setups**

440 Slice electrophysiology and *in vivo* experiments were performed using two setups capable of 3D scanless
441 holographic optogenetics with temporal focusing (3D-SHOT), as described previously (Mardinly et al.,
442 2018; Pégard et al., 2017; Sridharan et al., 2021). Both setups were custom-built on the Movable Objective
443 Microscope (MOM; Sutter Instrument Co.) platform, with three combined optical paths: a 3D two-photon
444 (2p) photostimulation path, a fast resonant-galvo raster scanning 2p imaging path, and a widefield one-
445 photon (1p) epifluorescence/IR-transmitted imaging path, merged by a polarizing beamsplitter before the

446 microscope tube lens and objective. In both setups, temporal focusing of the photostimulation beam from
447 the femtosecond fiber laser was achieved with a blazed holographic diffraction grating (33010FL01-520R
448 Newport Corporation). The beam was relayed through a rotating diffuser to randomize the phase pattern and
449 expand the temporally focused beam to cover the area of the high-refresh-rate spatial light modulator (SLM;
450 HSP1920-1064-HSP8-HB, 1920 × 1152 pixels, Meadowlark Optics). Holographic phase masks were
451 calculated using the Gerchberg-Saxton algorithm and displayed on the SLM to generate multiple
452 temporally-focused spots in 2D or 3D positions of interest (Gerchberg & Saxton, 1972). The
453 photostimulation path was then relayed into the imaging path with a polarizing beamsplitter placed
454 immediately prior to the tube lens. As described in Mardinly et al., 2018, to limit imaging artifacts
455 introduced by the photostimulation laser, the photostimulation laser was synchronized to the scan phase of
456 the resonance galvos using an Arduino Mega (Arduino), gated to be only on the edges of every line scan.
457 The setup for *in vitro* characterization of Ai203 and 2P synaptic connectivity mapping used a
458 Monaco 1035-80-60 737 (1040nm, 1MHz, 300fs, Coherent Inc.) for photostimulation and a Mai Tai
459 Ti:sapphire laser (Spectra Physics Inc.) for 2p calcium imaging. For *in vivo* characterization of Ai203 mice,
460 a similar setup was used except for a Monaco 1035-80-40 (1035nm, 2MHz, 276 fs, Coherent Inc.) was used
461 for photostimulation, and a Chameleon Ultra Ti:sapphire laser (Coherent Inc.) was used for 2p calcium
462 imaging.

463 ***In vitro* electrophysiology**

464 *In vitro* slice recordings were performed on 300µm-thick coronal slices from both male and female
465 mice aged P12-P30 (calcium sensor characterization) or P21-P42 (opsin characterization, and synaptic
466 connectivity mapping experiments). Slice preparation was done as previously described (Pégard et al.,
467 2017). Whole-cell patch-clamp protocols were performed in inline heating-controlled (33°C) standard
468 ACSF bath solution (in mM: NaCl 119, $NaHCO_3$ 26, Glucose 20, KCl 2.5, CaCl 2.5, $MgSO_4$ 1.3, NaH_2PO_4
469 1.3). Patch pipette (4-7 MOhm) were pulled from borosilicate glass filaments (Sutter Instrument Co.) and
470 filled with potassium (K)-gluconate solution (GCamp7s characterization; in mM: 110 K-gluconate, 10
471 HEPES, 1 EGTA, 20 KCl, 2 $MgCl_2$, 2 Na-ATP, 0.25 Na-GTP, 10 Phosphocreatine, 295 mOsm, pH=7.45)
472 or Cesium (Cs2+)-based internal solution (opsin characterization, and synaptic connectivity mapping
473 experiments; in mM: 135 $CeMeSO_4$, 3 NaCl, 10 HEPES, 0.3 EGTA, 4 Mg-ATP, 0.3 Na-GTP, 1 QX-314, 5
474 TEA-Cl, 295 mOsm, pH=7.45) also containing 50 µM Alexa Fluor hydrazide 488 or 594 dye
475 (ThermoFisher Scientific). Data was recorded at 20 kHz using 700b Multiclamp Axon Amplifier (Molecular
476 Devices). For loose-patch recordings the pipettes were filled with standard ACSF. The headstage with the
477 electrode holder (G23 Instruments) was controlled by Motorized Micromanipulator (MP285A; Sutter
478 Instrument Co.). All data was acquired and analyzed with custom code written in Matlab using the National
479 Instruments Data Acquisition (DAQ) Toolbox (NI). Membrane (Rm) and series (Rs) resistance were
480 monitored before and throughout experiments to ensure quality of acquired data. Cells were excluded if
481 initial access resistance was over 30 MOhm or if access resistance changed more than 30% during the
482 experiment, cells were excluded.
483

484 ***In vitro* characterization of opsin response characteristics**

485 For 1p characterization, setup and methods were identical to those described for 1p characterization
486 in Sridharan et al 2021.
487 For 2p characterization, cells positive for st-ChroME-GCaMP7s were identified through
488 fluorescence from widefield one-photon illumination using a Spectra X light engine (Lumencor). For both
489 measurements of 2P-photoactivated peak currents (whole-cell voltage clamp) and spiking (loose-patch), the

width of photostimulation was 5 ms. To measure peak 2P evoked photocurrents, a single holographic spot was aligned to a cell patched in whole-cell configuration and held in voltage clamp (-70mV) and stimulated across a series of laser powers (4.5, 7, 9, 13.5, 22.5, 45 mW) at 2 Hz. To measure spike probability, a cell in loose-patch configuration was stimulated with a single spot across laser powers (4.5, 7, 9, 11, 13.5, 22.5 mW) at different frequencies (5, 20, 40, 60 Hz). Stimulation conditions were randomized across an experiment.

The effective spatial resolution of photostimulation was measured in st-ChroME-GCaMP7s+ cells via loose-patch. We then measured spiking in response to photostimulation in the space surrounding the target cell by creating a voxelized three-dimensional volume spanning 97.5 × 97.5 × 50 µm in lateral and axial dimensions and at 6.5 × 6.5 × 12.5 µm per voxel. Spike probability was measured per stimulation of a voxel, then mapped according to the spatial location where the values were obtained. Lateral (x, y) and axial (z) physiological point-spread functions (PPSF) were quantified along grid planes where the highest spike probabilities per stimulated voxel were obtained. The spatial resolution at both lateral and axial dimensions were quantified as the full-width half-maximum (FWHM) of Gaussian profiles fitted to the PPSFs.

***In vitro* Imaging**

For GCaMP characterization (Fig. 2), GCaMP7s positive cells were identified in 1P or 2P illumination and patched. After establishing stable access, cell parameters (Rm, Rs) were logged and 5 ms duration step current pulses of increasing amplitude were used to determine neuron rheobase. A train of 1, 2, 3, 5, 10, 15, 20 or 30 action potentials were triggered at 30 Hz, using 5 ms duration current pulses 25 pA higher than rheobase while simultaneously imaging calcium fluorescence at a 30 Hz frame rate. Similar imaging laser power was used (35 mW) for all cells. For holographic stimulation during imaging, a power curve was taken to determine the minimum light power needed to reliably evoke spiking. Cells were stimulated with trains of 0, 1, 3, 5, or 10 5 ms holographic pulses at 30 Hz while simultaneously imaging and recording electrically. Only cells which reliably had holographically-induced spikes (>90% of trials with one spike per holographic pulse) were included in analysis. Imaging analysis is described with *in vivo* analysis.

Crosstalk characterization was performed as previously described (Sridharan et al., 2021), measured across FOV sizes (980 680 527µm), imaging frequencies (6, 10, 30 Hz), and powers (10, 15, 25, 35, 45 mW). Imaging frequencies were obtained by scanning the FOV at 30Hz while using the Pockels cell (Conoptics) to gate the scanning laser every n-th frame corresponding to frequency of interest. Cells were kept at resting potential throughout the protocol. Each trial consisted of a baseline period before two seconds of a scanning period. Only the cells with stable resting potential (<4 mV change) over the protocol were accepted for data analysis. Data obtained were baseline-subtracted, then median-filtered to remove action potentials.

***In vitro* Synaptic Connectivity Mapping**

Cells negative for st-ChroME-GCaMP7s (absence of fluorescence under 1P-illumination) were patched in whole-cell configuration and held at -70 mV. Preliminary assessment of photostimulation evoked postsynaptic responses and latency were done through widefield 1P stimulation at saturating power. To map synaptic inputs to the patched cell, the surrounding volume of 162.5 ×162.5 µm in lateral (x, y) and 100 µm in axial (z) dimensions was probed through holographic photostimulation of a precomputed three-dimensional grid of holographic spots. Each point (voxel) of photostimulation was spaced 6.5 × 6.5 × 25 (x, y, z) µm apart and were targeted randomly at 30 or 40 Hz with 5 ms laser pulses across 20 trials per laser power tested. Postsynaptic EPSCs within 25 ms time windows from the start of photostimulation at each

voxel were collected and sorted. Synaptic connectivity maps were generated by plotting the peak of mean EPSCs according to the spatial location of the corresponding voxels.

Viral Injection and Surgical Procedures

For comparison with Ai203 reporter mice, double transgenic mice expressing CaMKII-tTA;tetO-GCaMP6s (Wekselblatt et al., 2016) were crossed with transgenic SST-Cre (Taniguchi et al., 2011) or PV-Cre (Hippenmeyer et al., 2005) mice to create triple-transgenic mice expressing GCaMP6s in excitatory (tTA-expressing) neurons. Mice were intracranially injected with PhP.eB-TRE-ChroME-P2A-H2B-mRuby3, as previously described (Mardinly et al., 2018). Notably, as the tetracycline response element (TRE) viral promoter drives expression in cells expressing tetracycline trans-activator (tTA) (Gossen et al., 1995), viral transduction was coincident with excitatory neurons transgenically expressing GCaMP6s, and not dependent on the particular Cre line used (PV-Cre or SST-Cre).

Mice 6 weeks or older were anesthetized with 2% isoflurane and administered 2 mg/kg of dexamethasone (to reduce cerebral edema) and 0.5 mg/kg of buprenorphine (as an analgesic). Mice were then secured in a stereotaxic frame (Kopf) and kept warm with a heating pad. A small incision was made to expose the skull and 2 burr holes were placed over left V1 (3.4 mm lateral, 1 mm anterior of lambda) approximately 1 mm apart. 300 nL of virus was slowly injected between 200-300 µm below the dura, at a rate of 50 nL/s using a microinjector (Micro4; World Precision Instruments) and a glass pipette (Drummond Scientific). The glass pipette was kept in place for 5-10 minutes after injection to ensure adequate spread and prevent backflow of virus during retraction of the pipette. Headplating and cranial windowing (below) were performed immediately after viral injection.

Mice were headplated with custom-made titanium headplates. To ensure secure placement, the skull was lightly etched with a scalpel and the headplate was initially attached over V1 with Vetbond (3M). Metabond (C&B) and OrthoJet (Lang Dental) were used to permanently attach and secure the headplate. A craniotomy was made over the injection sites and V1 using a 3.5 mm biopsy punch. Once the skull was removed, bleeding was controlled with cold phosphate-buffered saline and Gelfoam (Pfizer Inc.). A cranial window was constructed by gluing together two 3 mm diameter circular coverslips to the bottom of a 5 mm diameter circular coverslip, then placed onto the craniotomy, and secured into place with Metabond (C&B). Mice were allowed to recover in a heated recovery cage.

***In vivo* Imaging and Photostimulation**

For 2-photon calcium imaging *in vivo*, mice were head-fixed and allowed to run on a freely moving circular treadmill under a 20X magnification (1.0 NA) water-immersion objective (Olympus Corporation) and imaged with a Sutter MOM 2p resonance scanning microscope controlled with MATLAB-based ScanImage software (Vidrio Technologies) (see also microscope design, above). Fast, 3 or 4 z-plane volumetric imaging (3 planes: 6.36 Hz, 4 planes: 4.77 Hz, field-of-view: 800 µm x 800 µm) was accomplished using an electrically-tunable lens (Optotune) placed in the light path prior to the resonance scanners. A 20 ms delay was added to the Y-galvo flyback time to provide adequate settle-time for the ETL and ensure a non-distorted field-of-view (FOV). Z-planes were placed 20 or 30 µm apart for 4 or 3 plane recordings, respectively. The imaging laser (Chameleon; Coherent Inc.) was tuned to 920 nm and restricted to <75 mW average power to limit scanning-induced crosstalk.

ChroME-expressing cells were identified by nuclear-localized mRuby3 fluorescence imaged at 1040 nm and using a custom 2d-peak detection algorithm in MATLAB. Detected cell locations were used as targets for holographic photostimulation. Custom written MATLAB code was used to synchronize the experiment via NI data acquisition boards. Visual stimuli were presented on a 2048 x 1536 Retina iPad LCD

display (Adafruit Industries) placed 10 cm from the mouse. The monitor backlight was synchronized with the galvos such that it came on only during the turnaround time, so that light from the monitor did not contaminate 2p imaging. Visual stimuli were created and presented with custom MATLAB code and Psychophysics ToolBox. drifting gratings (50 visual degrees, 1 Hz, .08 cycles per degree, 100% contrast) of different orientations were randomly presented for 1 second each trial and interleaved with a grey-screen ("blank") condition. Neurons with significantly different responses to visual stimuli ($p<0.05$, 1-way ANOVA) were considered as visually responsive. FOVs with fewer than 20% visually responsive cells were considered unlikely to be in V1 and excluded from further analysis. Preferred orientation was calculated as the max response from trial-averaged orientation tuning curves; orthogonal orientation was determined as the response 90 degrees from preferred orientation. Orientation selectivity index (OSI) was then calculated as:

$$OSI = \frac{PO_{mean} - OO_{mean}}{PO_{mean} + OO_{mean}}$$

Where PO is the mean response to preferred orientation and OO is the mean response to orthogonal orientation. Orientation tuning curves were min subtracted prior to OSI calculation to ensure values ranged from 0-1.

Calcium Imaging Post-Processing and Analysis

Calcium imaging data was extracted from raw TIFF files, motion corrected, and source-extracted using Suite2p (Pachitariu et al., 2017). Putative sources were manually curated based on morphology and fluorescence statistics. Neuropil traces for each source were generated by Suite2p, multiplied by a correction coefficient (0.7), and subtracted from source fluorescence traces. For each cell, calcium traces were minimum subtracted and a 1-minute rolling 20% quantile was used to calculate baseline fluorescence. A z-scored ΔF/F was then calculated as:

$$\Delta F/F = zscore\left(\frac{F - F_0}{F_0}\right)$$

Where F is a cell's fluorescence response and F_0 is baseline fluorescence. Individual trialwise responses were baseline subtracted using the mean pre-stimulus (holographic or visual) activity.

Holographic targets were matched to sources identified by Suite2p by the source satisfying the $argmin$ Euclidean distance for each target. Targets lacking a source within 15 µm were excluded from further analysis. In the rare cases where multiple targets matched to the same source, only the closest target was used. Cells were considered to be "stimmable" if their mean response to holographic stimulation was significantly different ($p<0.05$, one-tailed rank-sum) from baseline.

For *in vitro* characterization in Figure 2, F_0 was set to be the mean fluorescence one second pre-stimulus. For current injection, zero stimulation trials were simulated by taking fluorescence from the inter-trial interval of one spike trials, six seconds after the last spike stimulation. Mean calcium traces were calculated by taking the mean calcium trace across all trials for a given spike number for a given cell. Peak ΔF/F was the peak of the mean calcium trace, with the peak ΔF/F for 0 spike trials subtracted to account for noise. Decay time was calculated fitting the cross-trial mean calcium trace for a cell with a univariate spline, and the time from peak to ½ of peak fluorescence for the fit was taken as the half-decay. Only cells with peak ΔF/F >=.7 for 10 spikes were used for decay calculation to minimize noise.

Contrast Detection Task: Apparatus, Behavioral Training, and Task Design

Apparatus: The visual behavioral apparatus for the contrast detection task was controlled using an Arduino DUE synchronized with Raspberry Pi 3+/4+, which interfaced with a custom-written code in Python, Arduino and Java. Mouse licking was detected by changes in the capacitive load using a capacitive touch sensor (Adafruit, AT42QT1070) forming a circuit between the 0.05-inch diameter steel lickport and the mouse's tongue. Water was delivered by gravity though the lick port using a 2- way normally closed isolation valve control (Neptune Research Inc.). Visual stimuli were generated using a custom-written code in Python and presented using a gamma corrected LCD monitor (Podofo, 15.7 x 8.9 cm, 1024x600 pixels, 60 Hz refresh rate) located 12 cm from the right eye. The entire apparatus was mounted on an 8.0 x 8.0 x 0.5 inch (MB8; Thorlabs Inc.) aluminum breadboard and enclosed in a light isolation box (80/20).

Behavioral Training: Training began after headplate and cranial window implantation surgery, recovery (7 days) and water restriction (5-8 days). Prior to training, mice were habituated to head fixation in the tube apparatus with the monitor on. The habituation sessions were performed for 2 days lasting ~30 minutes each. The training schedule was divided into four main stages. During the first stage of behavioral training, head fixed mice were classically conditioned to lick in response to the presence of a visual stimulus consisting of a square patch of a drifting sinusoidal grating (2Hz, 0.08 cycles/degree, 600 ms, 100% contrast, 34 visual degrees, black background luminescence). On every trial, the visual stimulus was paired with a water reward delivered at the beginning of the response window. No catch trials occurred in this stage. Once mice reliably licked correctly within the response window in more than 80% of the trials, they moved onto the operant conditioning phase of training.

During the second stage of training, mice were trained to respond in the presence of the visual stimulus. Catch trials were introduced as 25% of trials. The mouse must lick in response to the visual stimulus within the reward window to receive a water reward and withhold licking otherwise to avoid time out punishments. Mice started this paradigm with the same visual stimuli features as stage 1(100% contrast, 34 VD, black background luminescence). Once mice reached performance criteria (>90% hit rate and <30% false alarm rate) for two consecutive days, mice were transitioned to stage three.

In stage three, background luminescence was ramped up until it reached mean luminance, then stimulus size was ramped down until it reached 18 VD. Ramping occurred within and across sessions as long as performance criteria were maintained. Once ramping was complete, mice had to maintain performance at criteria for one day to progress to the next stage.

In stage four, mice had to detect stimuli of varying contrasts. For strain comparisons (Fig. 4B-C), 10 different contrasts (not including 0% catch trials) were used and catch trials were 7.5% of all trials. For optogenetic testing (Fig. 4D-E), six different contrasts were used and catch trials were 25% of all trials.

In the fourth stage of training, mice started to detect visual stimuli with six different contrasts, customized for each mouse, to provide a reliable behavioral threshold. Stimuli of different contrasts were randomly interleaved within blocks. Catch trials represented 12% of the trials.

Task Design: The contrast detection task consisted of uncued GO or CATCH trials that occurred after random intertrial intervals (3-8 seconds). A no lick period was enforced in the two seconds preceding the trial, licking during this period caused a time-out punishment (5-9 seconds). In GO trials a visual stimulus of variable contrast was presented, if the mouse responded within the 500 ms response window, it received a reward. CATCH trials had identical timing, but no stimulus was presented and if the mouse licked within the response window it received a time out punishment. Time outs were 5-9 seconds. The 500 ms response

window immediately followed the 600 ms stimulus presentation. Contrasts were presented in randomly shuffled blocks wherein each contrast must occur three times.

Strain information: Wildtype mice were either C57BL/6J (2 mice) or F1 C57BL/6J x ICR hybrids (3 mice). No difference between these two strains was observed so data was combined between them. Camk2a-tTA;tetO-GCaMP6s mice were double transgenic heterozygotes.

One-Photon Optogenetic Stimulation

One-photon (1p) photostimulation during contrast detection task was delivered using an optical fiber (400µm diameter, 0.39 nA; Thorlabs Inc.) coupled to a 470-nm LED (M470F3, Thorlabs) driven by an LED driver (LEDD1B; Thorlabs Inc.) and positioned using a micromanipulator over the location of V1 at the posterior of the window. Light power was calibrated at the end of the fiber using a power meter (PM160T, Thorlabs). Stimulation power was calibrated to each mouse and ranged from 0.05-0.4 mW out of the fiber. To prevent photostimulation from interfering with behavioral performance, we attached a custom designed light-blocking cone to the mouse head and illuminated blue LED masking lights during the entire session. To further reduce any extraneous cues, we covered the left eye with a plastic eye patch. Light was delivered from the onset of the stimulus to the end of the response window on 33% of trials.

Adesnik, H., & Abdeladim, L. (2021). Probing neural codes with two-photon holographic optogenetics. In *Nature Neuroscience*. Nat Neurosci. https://doi.org/10.1038/s41593-021-00902-9

Andermann, M. L., Gilfoy, N. B., Goldey, G. J., Sachdev, R. N. S., Wölfel, M., McCormick, D. A., Reid, R. C., & Levene, M. J. (2013). Chronic Cellular Imaging of Entire Cortical Columns in Awake Mice Using Microprisms. *Neuron*, *80*(4), 900–913. https://doi.org/10.1016/j.neuron.2013.07.052

Andrasfalvy, B. K., Zemelman, B. V, Tang, J., & Vaziri, A. (2010). Two-photon single-cell optogenetic control of neuronal activity by sculpted light. *Proceedings of the National Academy of Sciences of the United States of America*, *107*(26), 11981–11986. https://doi.org/10.1073/pnas.1006620107

Baker, C. A., Elyada, Y. M., Parra, A., & Bolton, M. M. L. (2016). Cellular resolution circuit mapping with temporal-focused excitation of soma-targeted channelrhodopsin. *ELife*. https://doi.org/10.7554/eLife.14193

Bègue, A., Papagiakoumou, E., Leshem, B., Conti, R., Enke, L., Oron, D., & Emiliani, V. (2013). Two-photon excitation in scattering media by spatiotemporally shaped beams and their application in optogenetic stimulation. *Biomedical Optics Express*, *4*(12), 2869–2879. https://doi.org/10.1364/BOE.4.002869

Carrillo-Reid, L., Han, S., Yang, W., Akrouh, A., & Yuste, R. (2019). Controlling Visually Guided Behavior by Holographic Recalling of Cortical Ensembles. *Cell*. https://doi.org/10.1016/j.cell.2019.05.045

Carrillo-Reid, L., Yang, W., Bando, Y., Peterka, D. S., & Yuste, R. (2016). Imprinting and recalling cortical ensembles. *Science*, *353*(6300), 691–694. https://doi.org/10.1126/science.aaf7560

Chen, I. W., Ronzitti, E., Lee, B. R., Daigle, T. L., Dalkara, D., Zeng, H., Emiliani, V., & Papagiakoumou, E. (2019). In Vivo submillisecond two-photon optogenetics with temporally focused patterned light. *Journal of Neuroscience*, *39*(18), 3484–3497. https://doi.org/10.1523/JNEUROSCI.1785-18.2018

Chen, Y., Jang, H., Spratt, P. W. E., Kosar, S., Taylor, D. E., Essner, R. A., Bai, L., Leib, D. E., Kuo, T. W., Lin, Y. C., Patel, M., Subkhangulova, A., Kato, S., Feinberg, E. H., Bender, K. J., Knight, Z. A., & Garrison, J. L. (2020). Soma-Targeted Imaging of Neural Circuits by Ribosome Tethering. *Neuron*, *107*(3), 454-469.e6. https://doi.org/10.1016/j.neuron.2020.05.005

Chettih, S. N., & Harvey, C. D. (2019). Single-neuron perturbations reveal feature-specific competition in V1. *Nature*, *567*(7748). https://doi.org/10.1038/s41586-019-0997-6

Cone, J. J., Bade, M. L., Masse, N. Y., Page, E. A., Freedman, D. J., & Maunsell, J. H. R. (2020). Mice Preferentially Use Increases in Cerebral Cortex Spiking to Detect Changes in Visual Stimuli. *Journal*

of Neuroscience, *40*(41), 7902–7920. https://doi.org/10.1523/JNEUROSCI.1124-20.2020

Daie, K., Svoboda, K., & Druckmann, S. (2021). Targeted photostimulation uncovers circuit motifs supporting short-term memory. *Nature Neuroscience*, *24*(2), 259–265. https://doi.org/10.1038/s41593-020-00776-3

Daigle, T. L., Madisen, L., Hage, T. A., Valley, M. T., Knoblich, U., Larsen, R. S., Takeno, M. M., Huang, L., Gu, H., Larsen, R., Mills, M., Bosma-Moody, A., Siverts, L. A., Walker, M., Graybuck, L. T., Yao, Z., Fong, O., Nguyen, T. N., Garren, E., … Zeng, H. (2018). A Suite of Transgenic Driver and Reporter Mouse Lines with Enhanced Brain-Cell-Type Targeting and Functionality. *Cell*, *174*(2), 465-480.e22. https://doi.org/10.1016/j.cell.2018.06.035

Dalgleish, H. W. P., Russell, L. E., Packer, A. M., Roth, A., Gauld, O. M., Greenstreet, F., Thompson, E. J., & Häusser, M. (2020). How many neurons are sufficient for perception of cortical activity? *ELife*, *9*, 1–99. https://doi.org/10.7554/eLife.58889

Dana, H., Sun, Y., Mohar, B., Hulse, B. K., Kerlin, A. M., Hasseman, J. P., Tsegaye, G., Tsang, A., Wong, A., Patel, R., Macklin, J. J., Chen, Y., Konnerth, A., Jayaraman, V., Looger, L. L., Schreiter, E. R., Svoboda, K., & Kim, D. S. (2019). High-performance calcium sensors for imaging activity in neuronal populations and microcompartments. *Nature Methods*, *16*(7), 649–657. https://doi.org/10.1038/s41592-019-0435-6

Forli, A., Vecchia, D., Binini, N., Succol, F., Bovetti, S., Moretti, C., Nespoli, F., Mahn, M., Baker, C. A., Bolton, M. M., Yizhar, O., & Fellin, T. (2018). Two-Photon Bidirectional Control and Imaging of Neuronal Excitability with High Spatial Resolution In Vivo. *Cell Reports*. https://doi.org/10.1016/j.celrep.2018.02.063

Gerchberg, R. W., & Saxton, W. O. (1972). A Practical Algorithm for the Determination of Phase from Image and Diffraction Plane Pictures. *Optik*, *35*, 237–246.

Gill, J. V., Lerman, G. M., Zhao, H., Stetler, B. J., Rinberg, D., & Shoham, S. (2020). Precise Holographic Manipulation of Olfactory Circuits Reveals Coding Features Determining Perceptual Detection. *Neuron*, *0*(0). https://doi.org/10.1016/j.neuron.2020.07.034

Glickfeld, L. L., Histed, M. H., & Maunsell, J. H. R. (2013). Mouse Primary Visual Cortex Is Used to Detect Both Orientation and Contrast Changes. *Journal of Neuroscience*, *33*(50), 19416–19422. https://doi.org/10.1523/JNEUROSCI.3560-13.2013

Goldey, G. J., Roumis, D. K., Glickfeld, L. L., Kerlin, A. M., Reid, R. C., Bonin, V., Schafer, D. P., & Andermann, M. L. (2014). Removable cranial windows for long-term imaging in awake mice. *Nature Protocols*, *9*(11), 2515–2538. https://doi.org/10.1038/nprot.2014.165

Gossen, M., Freundlieb, S., Bender, G., Müller, G., Hillen, W., & Bujard, H. (1995). Transcriptional activation by tetracyclines in mammalian cells. *Science*, *268*(5218), 1766–1769. https://doi.org/10.1126/SCIENCE.7792603

Haery, L., Deverman, B. E., Matho, K. S., Cetin, A., Woodard, K., Cepko, C., Guerin, K. I., Rego, M. A., Ersing, I., Bachle, S. M., Kamens, J., & Fan, M. (2019). Adeno-Associated Virus Technologies and Methods for Targeted Neuronal Manipulation. *Frontiers in Neuroanatomy*, *13*. https://doi.org/10.3389/FNANA.2019.00093

Hage, T. A., Bosma-Moody, A., Baker, C. A., Kratz, M. B., Campagnola, L., Jarsky, T., Zeng, H., & Murphy, G. J. (2019). Distribution and strength of interlaminar synaptic connectivity in mouse primary visual cortex revealed by two-photon optogenetic stimulation. *BioRxiv*, 2019.12.13.876128. https://doi.org/10.1101/2019.12.13.876128

Harris, J. A., Hirokawa, K. E., Sorensen, S. A., Gu, H., Mills, M., Ng, L. L., Bohn, P., Mortrud, M., Ouellette, B., Kidney, J., Smith, K. A., Dang, C., Sunkin, S., Bernard, A., Oh, S. W., Madisen, L., & Zeng, H. (2014). Anatomical characterization of Cre driver mice for neural circuit mapping and manipulation. *Frontiers in Neural Circuits*, *0*(JULY), 76. https://doi.org/10.3389/FNCIR.2014.00076

Hippenmeyer, S., Vrieseling, E., Sigrist, M., Portmann, T., Laengle, C., Ladle, D. R., & Arber, S. (2005). A Developmental Switch in the Response of DRG Neurons to ETS Transcription Factor Signaling. *PLOS Biology*, *3*(5), e159. https://doi.org/10.1371/JOURNAL.PBIO.0030159

Jin, M., & Glickfeld, L. L. (2019). Contribution of Sensory Encoding to Measured Bias. *Journal of*

Neuroscience, *39*(26), 5115–5127. https://doi.org/10.1523/JNEUROSCI.0076-19.2019

Karnani, M. M., Jackson, J., Ayzenshtat, I., Sichani, A. H., Manoocheri, K., Kim, S., & Yuste, R. (2016). Opening Holes in the Blanket of Inhibition: Localized Lateral Disinhibition by VIP Interneurons. *Journal of Neuroscience*, *36*(12), 3471–3480. https://doi.org/10.1523/JNEUROSCI.3646-15.2016

Karnani, M. M., Jackson, J., Ayzenshtat, I., Tucciarone, J., Manoocheri, K., Snider, W. G. G., & Yuste, R. (2016). Cooperative Subnetworks of Molecularly Similar Interneurons in Mouse Neocortex. *Neuron*, *90*(1), 86–100. https://doi.org/10.1016/j.neuron.2016.02.037

Klapoetke, N. C., Murata, Y., Kim, S. S., Pulver, S. R., Birdsey-Benson, A., Cho, Y. K., Morimoto, T. K., Chuong, A. S., Carpenter, E. J., Tian, Z., Wang, J., Xie, Y., Yan, Z., Zhang, Y., Chow, B. Y., Surek, B., Melkonian, M., Jayaraman, V., Constantine-Paton, M., … Boyden, E. S. (2014). Independent Optical Excitation of Distinct Neural Populations. *Nature Methods*, *11*(3), 338. https://doi.org/10.1038/NMETH.2836

Lerman, G. M., Little, J. P., Gill, J. V., Rinberg, D., & Shoham, S. (2019). Real-Time In Situ Holographic Optogenetics Confocally Unraveled Sculpting Microscopy. *Laser and Photonics Reviews*, *13*(9), 1900144. https://doi.org/10.1002/lpor.201900144

Lim, S. T., Antonucci, D. E., Scannevin, R. H., & Trimmer, J. S. (2000). A Novel Targeting Signal for Proximal Clustering of the Kv2.1 K+ Channel in Hippocampal Neurons. *Neuron*, *25*(2), 385–397. https://doi.org/10.1016/S0896-6273(00)80902-2

Madisen, L., Garner, A. R., Shimaoka, D., Chuong, A. S., Klapoetke, N. C., Li, L., van der Bourg, A., Niino, Y., Egolf, L., Monetti, C., Gu, H., Mills, M., Cheng, A., Tasic, B., Nguyen, T. N., Sunkin, S. M., Benucci, A., Nagy, A., Miyawaki, A., … Zeng, H. (2015). Transgenic Mice for Intersectional Targeting of Neural Sensors and Effectors with High Specificity and Performance. *Neuron*, *85*(5), 942–958. https://doi.org/10.1016/J.NEURON.2015.02.022

Madisen, L., Mao, T., Koch, H., Zhuo, J. M., Berenyi, A., Fujisawa, S., Hsu, Y. W. A., Garcia, A. J., Gu, X., Zanella, S., Kidney, J., Gu, H., Mao, Y., Hooks, B. M., Boyden, E. S., Buzsáki, G., Ramirez, J. M., Jones, A. R., Svoboda, K., … Zeng, H. (2012). A toolbox of Cre-dependent optogenetic transgenic mice for light-induced activation and silencing. *Nature Neuroscience*, *15*(5), 793–802. https://doi.org/10.1038/nn.3078

Mardinly, A. R., Oldenburg, I. A., Pégard, N. C., Sridharan, S., Lyall, E. H., Chesnov, K., Brohawn, S. G., Waller, L., & Adesnik, H. (2018). Precise multimodal optical control of neural ensemble activity. *Nature Neuroscience*. https://doi.org/10.1038/s41593-018-0139-8

Marshel, J. H., Kim, Y. S., Machado, T. A., Quirin, S., Benson, B., Kadmon, J., Raja, C., Chibukhchyan, A., Ramakrishnan, C., Inoue, M., Shane, J. C., McKnight, D. J., Yoshizawa, S., Kato, H. E., Ganguli, S., & Deisseroth, K. (2019). Cortical layer-specific critical dynamics triggering perception. *Science*, *365*(6453). https://doi.org/10.1126/science.aaw5202

Miyashita, T., Shao, Y. R., Chung, J., Pourzia, O., & Feldman, D. E. (2013). Long-term channelrhodopsin-2 (ChR2) expression can induce abnormal axonal morphology and targeting in cerebral cortex. *Frontiers in Neural Circuits*, *7*, 8. https://doi.org/10.3389/fncir.2013.00008

Naka, A., Veit, J., Shababo, B., Chance, R. K., Risso, D., Stafford, D., Snyder, B., Egladyous, A., Chu, D., Sridharan, S., Mossing, D. P., Paninski, L., Ngai, J., & Adesnik, H. (2019). Complementary networks of cortical somatostatin interneurons enforce layer specific control. *ELife*. https://doi.org/10.7554/eLife.43696

Pachitariu, M., Stringer, C., Dipoppa, M., Schröder, S., Rossi, L. F., Dalgleish, H., Carandini, M., & Harris, K. D. (2017). Suite2p: beyond 10,000 neurons with standard two-photon microscopy. *BioRxiv*, 061507. https://doi.org/10.1101/061507

Packer, A. M., Peterka, D. S., Hirtz, J. J., Prakash, R., Deisseroth, K., & Yuste, R. (2012). Two-photon optogenetics of dendritic spines and neural circuits. *Nature Methods*, *9*(12), 1202–1205. https://doi.org/10.1038/nmeth.2249

Packer, A. M., Russell, L. E., Dalgleish, H. W. P., & Häusser, M. (2015). Simultaneous all-optical manipulation and recording of neural circuit activity with cellular resolution in vivo. *Nature Methods*, *12*(2). https://doi.org/10.1038/nmeth.3217

Papagiakoumou, E., Anselmi, F., Bègue, A., De Sars, V., Glückstad, J., Isacoff, E. Y., & Emiliani, V. (2010). Scanless two-photon excitation of channelrhodopsin-2. *Nature Methods*, *7*(10), 848–854. https://doi.org/10.1038/nmeth.1505

Papagiakoumou, E., Ronzitti, E., & Emiliani, V. (2020). Scanless two-photon excitation with temporal focusing. In *Nature Methods* (Vol. 17, Issue 6, pp. 571–581). Nature Publishing Group. https://doi.org/10.1038/s41592-020-0795-y

Pégard, N. C., Mardinly, A. R., Oldenburg, I. A., Sridharan, S., Waller, L., & Adesnik, H. (2017). Three-dimensional scanless holographic optogenetics with temporal focusing (3D-SHOT). *Nature Communications*, *8*(1), 1228. https://doi.org/10.1038/s41467-017-01031-3

Picot, A., Dominguez, S., Liu, C., Chen, I. W., Tanese, D., Ronzitti, E., Berto, P., Papagiakoumou, E., Oron, D., Tessier, G., Forget, B. C., & Emiliani, V. (2018). Temperature Rise under Two-Photon Optogenetic Brain Stimulation. *Cell Reports*, *24*(5), 1243-1253.e5. https://doi.org/10.1016/j.celrep.2018.06.119

Prakash, R., Yizhar, O., Grewe, B., Ramakrishnan, C., Wang, N., Goshen, I., Packer, A. M., Peterka, D. S., Yuste, R., Schnitzer, M. J., & Deisseroth, K. (2012). Two-photon optogenetic toolbox for fast inhibition, excitation and bistable modulation. *Nature Methods*, *9*(12), 1171–1179. https://doi.org/10.1038/nmeth.2215

Preibisch, S., Saalfeld, S., & Tomancak, P. (2009). Globally optimal stitching of tiled 3D microscopic image acquisitions. *Bioinformatics*, *25*(11), 1463. https://doi.org/10.1093/BIOINFORMATICS/BTP184

Rickgauer, J. P., Deisseroth, K., & Tank, D. W. (2014). Simultaneous cellular-resolution optical perturbation and imaging of place cell firing fields. *Nature Neuroscience*, *17*(12), 1816–1824. https://doi.org/10.1038/nn.3866

Robinson, N. T. M., Descamps, L. A. L., Russell, L. E., Buchholz, M. O., Bicknell, B. A., Antonov, G. K., Lau, J. Y. N., Nutbrown, R., Schmidt-Hieber, C., & Häusser, M. (2020). Targeted Activation of Hippocampal Place Cells Drives Memory-Guided Spatial Behavior. *Cell*, *183*(6), 1586-1599.e10. https://doi.org/10.1016/j.cell.2020.09.061

Ronzitti, E., Conti, R., Zampini, V., Tanese, D., Foust, A. J., Klapoetke, N. C., Boyden, E. S., Papagiakoumou, E., & Emiliani, V. (2017). Submillisecond optogenetic control of neuronal firing with two-photon holographic photoactivation of chronos. *Journal of Neuroscience*, *37*(44), 10679–10689. https://doi.org/10.1523/JNEUROSCI.1246-17.2017

Ronzitti, E., Emiliani, V., & Papagiakoumou, E. (2018). Methods for three-dimensional all-optical manipulation of neural circuits. In *Frontiers in Cellular Neuroscience*. https://doi.org/10.3389/fncel.2018.00469

Ruediger, S., & Scanziani, M. (2020). Learning speed and detection sensitivity controlled by distinct cortico-fugal neurons in visual cortex. *ELife*, *9*, 1–24. https://doi.org/10.7554/ELIFE.59247

Shemesh, O. A., Linghu, C., Piatkevich, K. D., Goodwin, D., Celiker, O. T., Gritton, H. J., Romano, M. F., Gao, R., Yu, C. C. (Jay), Tseng, H. A., Bensussen, S., Narayan, S., Yang, C. T., Freifeld, L., Siciliano, C. A., Gupta, I., Wang, J., Pak, N., Yoon, Y. G., … Boyden, E. S. (2020). Precision Calcium Imaging of Dense Neural Populations via a Cell-Body-Targeted Calcium Indicator. *Neuron*, *107*(3), 470-486.e11. https://doi.org/10.1016/j.neuron.2020.05.029

Shemesh, O. A., Tanese, D., Zampini, V., Linghu, C., Piatkevich, K., Ronzitti, E., Papagiakoumou, E., Boyden, E. S., & Emiliani, V. (2017). Temporally precise single-cell-resolution optogenetics. *Nature Neuroscience*, *20*(12), 1796–1806. https://doi.org/10.1038/s41593-017-0018-8

Sridharan, S., Gajowa, M., Ogando, M. B., Jagadisan, U., Abdeladim, L., Sadahiro, M., Bounds, H., Hendricks, W. D., Tayler, I., Gopakumar, K., Oldenburg, I. A., Brohawn, S. G., & Adesnik, H. (2021). High performance microbial opsins for spatially and temporally precise perturbations of large neuronal networks. *BioRxiv*, 2021.04.01.438134. https://doi.org/10.1101/2021.04.01.438134

Taniguchi, H., He, M., Wu, P., Kim, S., Paik, R., Sugino, K., Kvitsani, D., Fu, Y., Lu, J., Lin, Y., Miyoshi, G., Shima, Y., Fishell, G., Nelson, S. B., & Huang, Z. J. (2011). A Resource of Cre Driver Lines for Genetic Targeting of GABAergic Neurons in Cerebral Cortex. *Neuron*, *71*(6), 995–1013. https://doi.org/10.1016/j.neuron.2011.07.026

Tasic, B., Menon, V., Nguyen, T. N., Kim, T. K., Jarsky, T., Yao, Z., Levi, B., Gray, L. T., Sorensen, S. A.,

Dolbeare, T., Bertagnolli, D., Goldy, J., Shapovalova, N., Parry, S., Lee, C., Smith, K., Bernard, A., Madisen, L., Sunkin, S. M., … Zeng, H. (2016). Adult mouse cortical cell taxonomy revealed by single cell transcriptomics. *Nature Neuroscience*, *19*(2), 335–346. https://doi.org/10.1038/nn.4216

Vong, L., Ye, C., Yang, Z., Choi, B., Chua, S., Jr., & Lowell, B. B. (2011). Leptin Action on GABAergic Neurons Prevents Obesity and Reduces Inhibitory Tone to POMC Neurons. *Neuron*, *71*(1), 142. https://doi.org/10.1016/J.NEURON.2011.05.028

Wekselblatt, J. B., Flister, E. D., Piscopo, D. M., & Niell, C. M. (2016). Large-scale imaging of cortical dynamics during sensory perception and behavior. *Journal of Neurophysiology*, *115*(6), 2852. https://doi.org/10.1152/JN.01056.2015

Wu, C., Ivanova, E., Zhang, Y., & Pan, Z. H. (2013). rAAV-Mediated Subcellular Targeting of Optogenetic Tools in Retinal Ganglion Cells In Vivo. *PLoS ONE*. https://doi.org/10.1371/journal.pone.0066332

Xue, Y., Waller, L., Adesnik, H., & Pégard, N. (2020). Three-dimensional Multi-site Random Access Photostimulation (3D-MAP). *BioRxiv*, 2020.06.28.176503. https://doi.org/10.1101/2020.06.28.176503

Yang, W., Carrillo-Reid, L., Bando, Y., Peterka, D. S., & Yuste, R. (2018). Simultaneous two-photon imaging and two-photon optogenetics of cortical circuits in three dimensions. *ELife*, *7*, e32671. https://doi.org/10.7554/eLife.32671